

NEARBY GALAXY FILAMENTS AND THE Ly α FOREST: CONFRONTING SIMULATIONS AND THE UV BACKGROUND WITH OBSERVATIONS*BART P. WAKKER^{1,4}, AUDRA K. HERNANDEZ^{1,4}, DAVID M. FRENCH^{1,4}, TAE-SUN KIM², BENJAMIN D. OPPENHEIMER³, AND BLAIR D. SAVAGE^{1,4}¹ Department of Astronomy, University of Wisconsin, Madison, WI 53706, USA; wakker@astro.wisc.edu, savage@astro.wisc.edu² Osservatorio Astronomico di Trieste, Via G.B. Tiepolo, 11, I-34143, Trieste, Italy³ CASA, Department of Astrophysical and Planetary Sciences, University of Colorado, Boulder, CO 80309, USA

Received 2015 May 6; accepted 2015 October 7; published 2015 November 16

ABSTRACT

Simulations of the formation of large-scale structures predict that dark matter, low density highly ionized gas, and galaxies form 10 to 40 Mpc scale filaments. These structures are easily recognized in the distribution of galaxies. Here we use Ly α absorption lines to study the gas in 30 \times 6 Mpc filament at $cz \sim 3500 \text{ km s}^{-1}$, defined using a new catalog of nearby ($cz < 10,000 \text{ km s}^{-1}$) galaxies, which is complete down to a luminosity of about $0.05 L_*$ for the region of space analyzed here. Using *Hubble Space Telescope* spectra of 24 active galactic nuclei, we sample the gas in this filament. All of our sightlines pass *outside* the virial radius of any known filament galaxy. Within 500 kpc of the filament axis the detection rate is $\sim 80\%$, but no detections are seen more than 2.1 Mpc from the filament axis. The width of the Ly α lines correlates with filament impact parameter and the four BLAs in our sample occur within 400 kpc of the filament axis, indicating increased temperature and/or turbulence. Comparing to simulations, we find that the recent Haardt & Madau extragalactic ionizing background predicts a factor of 3–5 too few ionizing photons. Using a more intense radiation field matches the hydrogen density profile within 2.1 Mpc of the filament axis, but the simulations still overpredict the detection rate between 2.1 and 5 Mpc from the axis. The baryonic mass inside filament galaxies is $1.4 \times 10^{13} M_\odot$, while the mass of filament gas outside galaxy halos is found to be $5.2 \times 10^{13} M_\odot$.

Key words: galaxies: halos – intergalactic medium – quasars: absorption lines – ultraviolet: general

1. INTRODUCTION

The current paradigm for the formation of large-scale structures holds that after the Big Bang, dark matter was concentrated by gravity into sheets, filaments, and halos. Observational (e.g., Fukugita & Peebles 2006; Shull et al. 2012; Danforth et al. 2014) and theoretical (e.g., Cen & Ostriker 1999; Davé et al. 2001; Smith et al. 2011; Cen 2013) studies suggest that the baryons are carried along, with a small fraction ($\sim 10\%$ at the present time) forming galaxies inside dark matter halos. The remaining baryons stay in the circumgalactic (CGM) and intergalactic (IGM) medium, with at $z = 0$ about $30 \pm 10\%$ in the form of photoionized hydrogen at 10^4 K (Penton et al. 2002; Lehner et al. 2007; Danforth & Shull 2008; Shull et al. 2012), and 40% to 60% at higher temperatures in the Warm-Hot Intergalactic Medium (WHIM). All these different processes result in the Cosmic Web of dark matter, galaxy, and gas filaments.

The galaxies represent a small fraction of the baryons. Because they are luminous and energetic, our understanding is relatively advanced. However, to fully understand the development of structure, we should also understand the 10 times more numerous (but more difficult to observe) baryons outside galaxies that are still in the IGM.

Hydrodynamical simulations can be used to describe the evolution of Ly α lines from high redshifts until the present. They predict the gradual disappearance of the Ly α forest from

$z = 3$ to $z = 0$, the increase in temperature of the IGM over time, and the nature of the association of intergalactic gas with galaxies (Davé et al. 1999). Simulations also predict that the optical depth of H I absorption is closely tied to the underlying overdensity of dark matter (e.g., Croft et al. 1998; Schaye 2001), and give a specific expectation for the hydrogen column density profile perpendicular to the dark matter filaments.

Observationally, the decrease in the number counts and column density of Ly α absorbers over time provides evidence for the theoretical picture of the IGM (e.g., Weymann et al. 1998; Kim et al. 2007, 2013; Rudie et al. 2013; Rahmati et al. 2013). Other *statistical* evidence comes from the spatial association between strong ($\log N(\text{H I}) > 14$) Ly α absorbers and galaxies (Morris & Januzzi 2006; Ryan-Weber 2006; Stone et al. 2010) and from the power spectrum of the Ly α absorbers (see e.g., Paschos et al. 2009; Lee et al. 2015 and references therein).

To turn the simulated hydrogen density into a prediction for the observable H I column density requires a prescription for the intensity of the ionizing flux in the extragalactic background (EGB). Until recently, the most widely used prescription was provided by Haardt & Madau (2001), based on the spectra and number density of quasars and galaxies and the evolution of those quantities over time. They updated their model in 2012 (Haardt & Madau 2012), but this later version has a much lower (a factor 3.7) ionizing flux at $z = 0$.

At $z = 0$ Davé et al. (2010) compared the simulated column density distribution of Ly α absorbers to the observations of Lehner et al. (2007), showing a relatively good fit. However, with the updated version for the EGB given by Haardt & Madau (2012) and a larger sample of low redshift Ly α absorbers (Danforth et al. 2014), Kollmeier et al. (2014)

* Based on observations taken by the NASA/ESA *Hubble Space Telescope*, obtained at the Space Telescope Science Institute, which is operated by the Association of Universities for Research in Astronomy, Incorporated, under NASA contract NAS5-26555.

⁴ Supported by NASA/NSF.

found that a factor of five times too few photons are produced to ionize the Ly α forest to the observed levels, by comparing the expected and observed column density distribution of Ly α absorbers. In this paper we confirm this deficit using a different method. The discrepancy was further analyzed by Khaire & Srianand (2015), who argued that the quasar contribution is higher by a factor of two, and additionally suggested a 4% escape fraction of Lyman continuum photons from star-forming galaxies to match the opacity inferred from the Ly α forest. Shull et al. (2015) used different simulations to reduce the H I column densities, probably due to extremely strong feedback and argued that the Haardt & Madau (2012) quasar emissivity combined with $\sim 5\%$ escape fraction will produce the observed Ly α forest.

Most of the effort to understand absorption lines from the IGM has gone into work on the CGM of galaxies (the gas within ~ 300 kpc), using ensemble studies of individual galaxy halos (see e.g., Morris et al. 1993; Lanzetta et al. 1995; Prochaska et al. 2006; Stocke et al. 2006; Wakker & Savage 2009; Rudie et al. 2012; Stocke et al. 2013; Tumlinson et al. 2013 and many references in those papers). Yet, the most visually striking prediction of the hydrodynamic simulations is the presence of large-scale filamentary structure. Such filamentary structure is clearly evident in the distribution of galaxies, but this gas has not been directly studied. Crosscuts through simulations (see e.g., Figure 2 in Lukić et al. 2015) clearly show these filaments in the H I distribution.

The possible presence of filaments can be suggested by looking at the distribution of Ly α absorbers in a single sightline. Morris et al. (1993) analyzed a deep galaxy sample within a degree of the 3C 273 sightline, combined with a shallower sample out to 10 Mpc. They found that the distribution of galaxies and absorbers as function of redshift shows definite peaks (indicating the presence of galaxy filaments), and that absorbers are not randomly distributed with respect to the galaxies; they also found absorbers that seemed to have no associated galaxies within 1 Mpc. In the same manner, Tripp et al. (1998) also showed that both absorbers and galaxies cluster around certain redshifts for the sightlines toward H 1821+643 and PG 1116+215.

Studies of the transverse distribution of Ly α absorbers with respect to the sightline are rare. Tejos et al. (2014) looked at the correlation between galaxies and absorbers in six fields toward QSOs with $z \sim 0.7$. However, they could only study the correlation function out to a few Mpc from each sightline. From this they concluded that 50% of weak H I absorbers reside in what they call “galaxy voids” (i.e., no substantial dark matter halo is present within a few Mpc of the absorber). However, they did not really map the distribution of absorbers relative to the structures seen in the galaxy distribution. Finally, Tejos et al. (2015) found some evidence for an enhanced detection rate of narrow, broad, and O VI absorption lines in regions between galaxy clusters (i.e., regions where filamentary gas is expected). This approach is complementary to the approach we will take in this paper, in that they study multiple filaments intersected along a single sightline, rather than filaments parallel to a set of sightlines. However, since they do not map the galaxies in these filaments, and therefore cannot determine the separations between their sightlines and the filament axes, the

question of possible associations between absorptions and galaxy halos remains more open.

At redshifts beyond about $10,000 \text{ km s}^{-1}$, mapping out the galaxies over large regions around individual sightlines is observationally expensive. The galaxies are relatively faint but still need to be mapped over many degrees, whereas instrumental limitations typically result in galaxy maps covering only about one degree around a sightline and larger-scale mapping is eschewed in favor of mapping multiple sightlines. At the lowest redshifts ($cz < 5000 \text{ km s}^{-1}$ or so), however, it is possible to get a mostly complete galaxy sample down to low luminosities ($0.1 L_*$ or lower) across most of the sky, because this luminosity corresponds to a galaxy with $m \sim 17$. Most of the sky has been covered this deeply, especially in regions covered by the footprint of surveys such as the Sloan Digital Sky Survey (SDSS) and the 6dF Galaxy Survey.

The potential of this approach was first shown in a study by Narayanan et al. (2010). They combined Ly α and O VI absorption at $cz \sim 3000 \text{ km s}^{-1}$ in the direction of the Seyfert galaxy Mrk 290 to show the presence of gas at a temperature of $1.4 \times 10^5 \text{ K}$ at an impact parameter of 475 kpc to the nearest large galaxy, NGC 5987. However, they also showed that this galaxy was located in a 30° ($\sim 30 \text{ Mpc}$) long T-shaped filament. With two other sightlines through the filament showing absorption at similar velocities, and three off-filament sightlines yielding non-detections, the interpretation of the absorber toward Mrk 290 as originating in the outer halo of NGC 5987 was thrown into doubt.

To follow up on this realization, we used the Cosmic Origins Spectrograph (COS) on the *Hubble Space Telescope* (HST) to obtain spectra for 17 additional active galactic nuclei (AGN) sampling the filament found by Narayanan et al. (2010). Supplementing these with seven archival sightlines, we describe how we used these data to develop a new approach to constraining the properties of the Ly α forest that uses the *spatial* distribution of the absorbers in relation to the location of the dark matter/galaxy filaments. To do so we first need to set up several independent pieces:

- a. Section 2 presents the galaxy filament found by Narayanan et al. (2010) and the details of the method that we used to objectively define the filament axis.
- b. Section 3 presents the selection of targets and our definition of a “filament impact parameter.”
- c. Section 4 concentrates on the description of simulations from which H I column densities can be derived, which are needed to interpret our results.

In addition, we describe our method to correct the wavelength scale of COS spectra in an [Appendix](#).

We combine all these items in Section 5, where we give the measurements on the spectra and discuss the galaxy/AGN impact parameters and the distribution of equivalent widths, column densities, and line widths as function of separation to the filament axis, both in terms of just observations and in terms of comparisons to the simulations. Specifically, we look at the influence of the assumed intensity of the EGB radiation and compare the predictions for the run of the detection fraction as function of the filament impact parameter to the observations.

2. THE GALAXY FILAMENT

2.1. Galaxy Sample and Impact Parameters

In this section we describe the galaxy filament we study and discuss the method we use to derive a “filament impact parameter,” in addition to the usual “galaxy impact parameter” that is commonly used when studying intergalactic absorption lines.

We base our definition of the galaxy filament on the NASA Extragalactic Database (NED), first retrieving all information for all galaxies with $cz < 10,000 \text{ km s}^{-1}$, finding their location on the sky, redshift, redshift-independent distance (if available), angular diameter, position angle, inclination, and type. This data set will be described in more detail in a future paper (D. M. French et al. 2015, in preparation). Much of the data for the galaxies found in NED originated from the RC3 (de Vaucouleurs et al. 1991), with updates from many individual papers in the years since. The two other main sources of photometry and redshift data for nearby galaxies are the 2MASS (Skrutskie et al. 2006) and SDSS (Abazajian et al. 2009) surveys. For many of these galaxies there have been multiple published measurements of recession velocities and diameters. We use the NED consensus value and refer the reader to the NED pages for each individual galaxy for the further details and references. Errors are given for the original measurements of recession velocities, and are typically on the order of $10\text{--}20 \text{ km s}^{-1}$. However, NED does not provide an error on the consensus velocity and we therefore do not include errors in our tables either.

Galaxy diameters were derived from angular diameters and individual galaxy distances. All angular diameter measurements were retrieved from NED. Diameters are preferentially taken from 2MASS K_s “total” surface brightness extrapolation diameter measurements (for about 50% of all galaxies in our sample). For galaxies with no 2MASS measurement, we plot different magnitudes against K_s “total” values, and make a simple least squared linear fit between these magnitudes to estimate K_s . SDSS diameters are available for $\sim 20\%$ of the sample, while for $\sim 27\%$ no diameter is given in NED. The remaining 3% of diameters are based on other surveys. To derive the 2MASS K_s diameters, the “total” aperture radius r_{tot} is defined as the point at which the surface brightness extends down to five disk scale lengths (see Jarrett et al. 2003 for a full description). The r_{tot} value is derived as $r_{\text{tot}} = r' + a(\ln 148)^b$, where r' is the starting point radius ($>5''\text{--}10''$ beyond the nucleus, essentially beyond the PSF and nuclear or core influence) and a and b are the scale length parameters from a Sérsic exponential function: $f = f_0 \exp(-r/a)^{1/b}$. The fit extends to the point at which the mean surface brightness in the elliptical annulus has signal-to-noise ratio (S/N) < 2 . We do not give errors on these final diameters, because they are not given by NED either.

Figure 1 shows the distribution of diameters and apparent B magnitudes of all galaxies in the region we analyze (R.A. $208^\circ\text{--}276^\circ$, decl. $41^\circ\text{--}72^\circ$, and recession velocity 2900 to 4300 km s^{-1} ; see Section 2.2). For 30% of the galaxies in the sample, B was measured directly, while for most of the rest we find B from the SDSS g and r values using $B = g + 0.39(g - r) + 0.21$ (Jester et al. 2005). Figure 1 also shows estimated luminosities and absolute magnitudes, which are based on the empirical scaling between luminosity (L/L_*) and diameter D found by Wakker & Savage (2009):

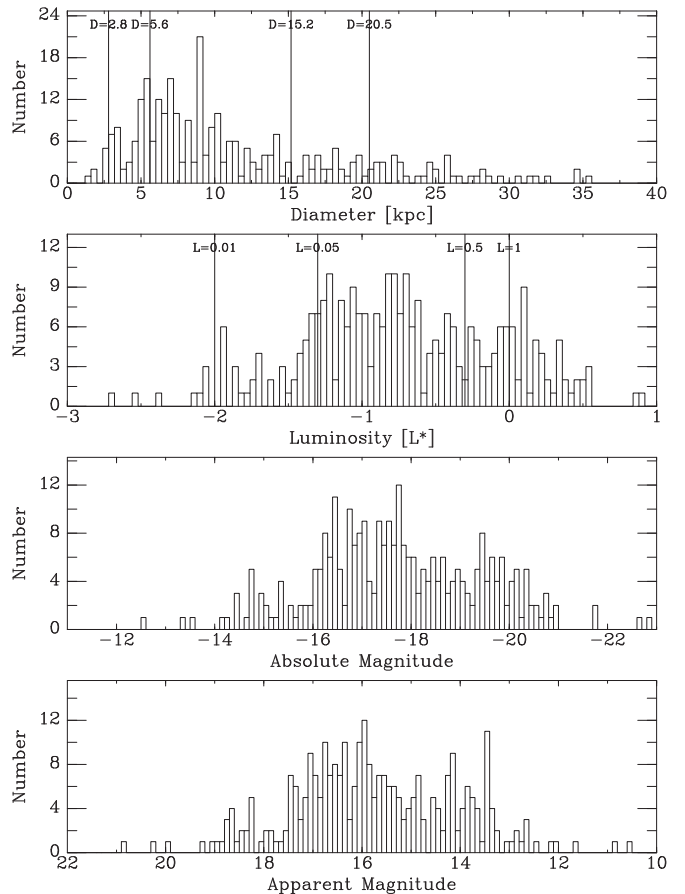


Figure 1. Histogram of implied galaxy diameters, observed apparent magnitudes, and derived luminosities and absolute magnitudes for the galaxies in the filament. This plot includes all 365 galaxies in the sky area shown in Figure 2. Diameters are mostly based on the 2MASS K-band angular diameters (see text), combined with the estimated galaxy distances. Luminosities follow from the empirical relation between luminosity and diameter found by Wakker & Savage (2009), which gives the luminosity to within a factor of 2. In the upper two panels, vertical lines indicate galaxies with $L = 0.01, 0.05, 0.5,$ and $1 L_*$.

$\log L = 2.31 \log D - 3.03$. This relation yields luminosities to within a factor ~ 2 . It gives $L = 0.05 L_*$ for $D = 5.6 \text{ kpc}$ and $L = 1 L_*$ for $D = 20.5 \text{ kpc}$. Using the fact that $M_B = -19.57$ for a L_* galaxy (Marzke et al. 1994), $L = 0.05 L_*$ corresponds to an apparent magnitude of 17.2 at a redshift $cz = 3500 \text{ km s}^{-1}$. It would be preferable to use observed magnitudes and distances to derive galaxy luminosities, but the data in NED is extremely inhomogeneous. We are working on a proper derivation of luminosity (D. M. French et al. 2015, in preparation), but preliminary numbers show that the distribution of luminosities will remain very similar.

Figure 1 shows that the number of galaxies increases down to a diameter of about 5 kpc (corresponding to a luminosity of $0.05 \sim L_*$; i.e., about the luminosity of the SMC), with a break at about that diameter/luminosity. That this limiting luminosity is relatively low is due to the fact that this area of the sky is in the footprint of the SDSS; about half of the galaxies in the filament had redshifts that were first measured by this survey. We note that for almost all galaxies brighter than $r = 17.7$, the SDSS provides spectroscopy and thus a redshift. Using the conversion given above, we find that this distribution of B magnitudes cuts off at $B \sim 18.5$. Given that $M_B^* = -19.57$, this corresponds to $0.01 L_*$ at 2900 km s^{-1} and $0.02 L_*$ at

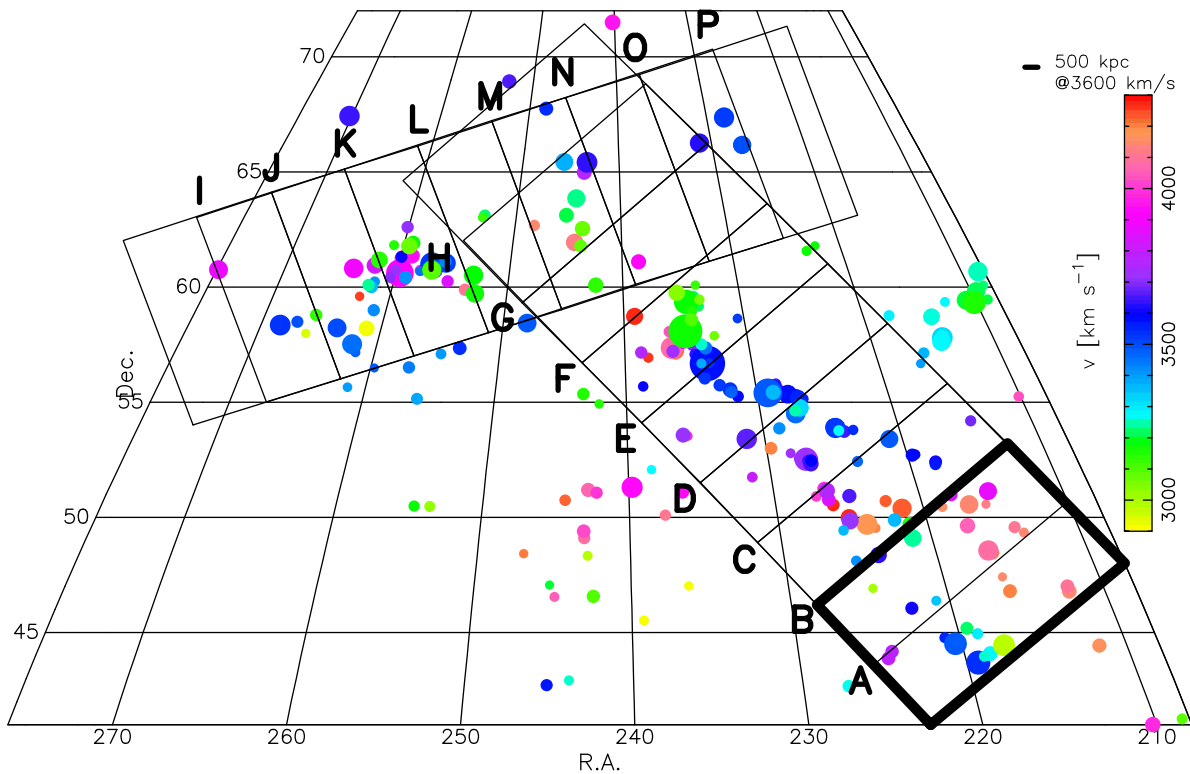


Figure 2. Distribution of galaxies (colored circles) in the galaxy filament. The sizes of the galaxy circles are proportional to their area, while the color indicates their velocities following the scale bar on the right. Note that only galaxies with velocities between 2900 and 4300 km s^{-1} are shown. The labeled rectangles show the strip boxes used to calculate the filament axis. Box A is outlined with a thick line as a reminder that these boxes overlap by 50%.

4300 km s^{-1} (i.e., when we are able to finalize a more direct derivation of luminosities, the implied completeness limit will be similar to that found from the diameter to luminosity conversion we use here). We conclude that our galaxy sample is mostly complete above $L = 0.05 L_*$.

We also estimate the virial radius of each galaxy, using the parametrization discussed by Stocke et al. (2013). This relates a galaxy’s luminosity to its virial radius. Figure 1 of Stocke et al. (2013) shows a number of relations between the virial radius and luminosity, which they use to derive a representative relation. This has a steeper slope at high luminosity than at low luminosity ($L < 0.1 L_*$). Because almost all our galaxies are brighter than $0.1 L_*$, we use the plot in Stocke et al. (2013) to approximate the average relation between the virial radius and luminosity as $\log R_{\text{vir}} = 0.3 \log L + 2.25$. Combining this with the Wakker & Savage (2009) empirical relation between galaxy diameter and luminosity shows that a galaxy’s virial radius can be approximated as $\log R_{\text{vir}} = 0.69 \log D + 1.24$.

2.2. Defining Filament Axes

Figure 2 shows all galaxies with R.A. between 208° and 276° , decl. between 41° and 72° , and recession velocity between 2900 and 4300 km s^{-1} . It is obvious that with this selection most galaxies (especially the ones with cz between ~ 3000 and $\sim 3700 \text{ km s}^{-1}$) are distributed along two mostly linear structures, which we interpret as a T-shaped galaxy filament.

Several papers have been written about algorithms to automatically find filaments in galaxy data sets (e.g., Sousbie 2011; Cautun et al. 2013; Tempel et al. 2014; Chen et al. 2015 and references in these papers). In particular, a priori one might

think that the catalog of galaxy filaments published by Tempel et al. (2014) could be used to define our filament, because that paper uses an algorithm to define filaments in the SDSS data. However, their catalog only contains a grand total of 90 galaxies that are brighter than $r = 17.7$ at distances $< 50 \text{ Mpc}$, and none of those are in the region of the sky where our filament occurs. In general, any SDSS-only based galaxy, group, cluster, or filament catalogs will not be useful to define filaments at redshifts $< 5000 \text{ km s}^{-1}$. A further reason that we do not use these codes is that we do not have access to them. In addition, many are optimized for finding filaments in simulations, but not in real (messier) galaxy data, which have issues like varying luminosity limits and large distance uncertainties when using the Hubble constant to convert velocities to distances. Until we can assess the usefulness of these various codes and algorithms, we proceed using the simpler, less general, but more intuitive method we developed ourselves, which is described below.

Our method is more limited than a general filament-finding algorithm in that we only look for filaments whose long axes are more or less parallel to the plane of the sky. This is not a problem, however, but rather a feature, because otherwise it would not be possible to determine where the absorption lines in some velocity range fall relative to the filament. For instance, a 10 Mpc long filament that is mostly perpendicular to the plane of the sky would show associated absorption over a 7000 km s^{-1} range, and it would be difficult to interpret these lines; it also would not be possible to determine a useful impact parameter to the filament. Mostly parallel filaments present the cleanest cases.

(1) First we draw two rectangular boxes on the sky map and divide these into 6 Mpc “strips” along the filament axis, using a

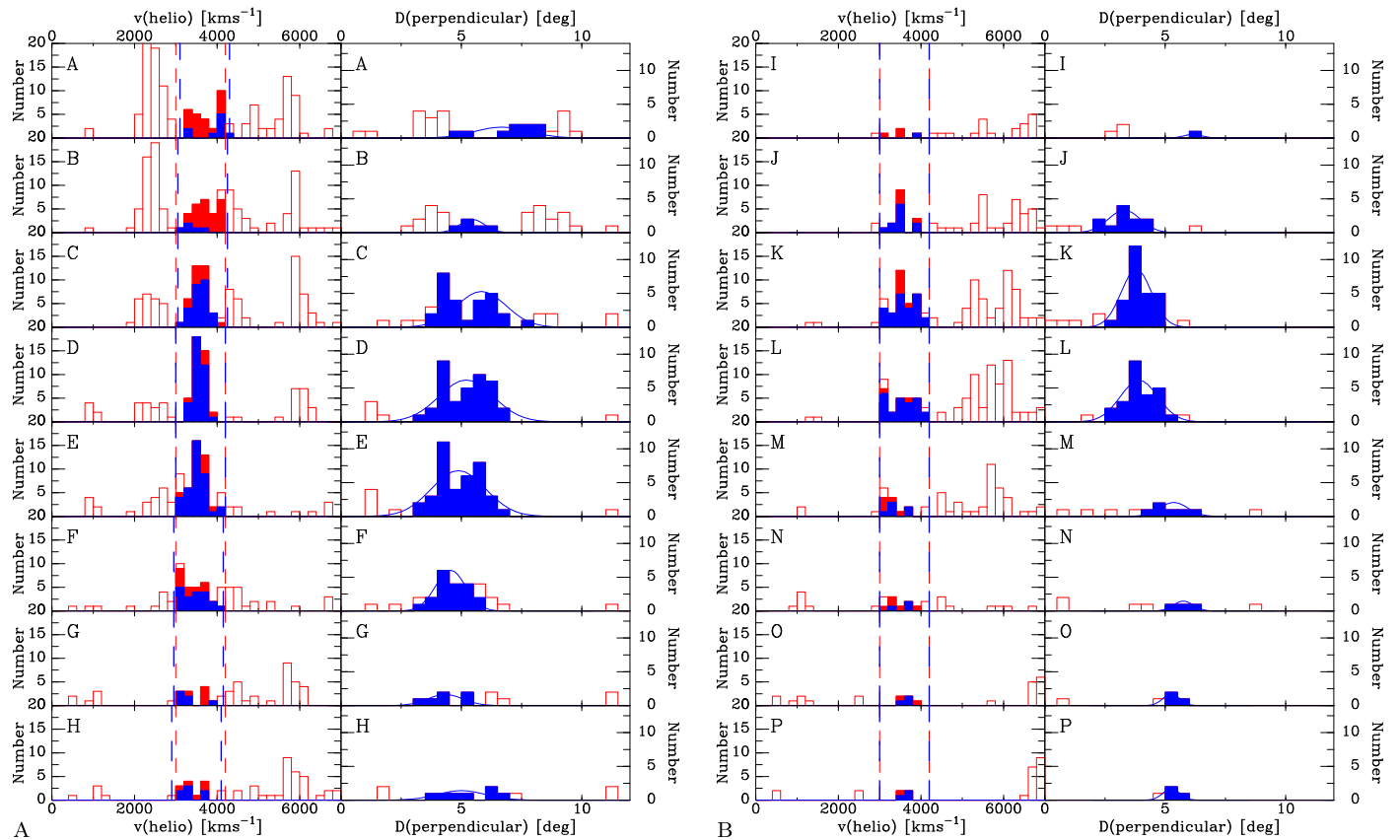


Figure 3. The red histograms in the left panels give the velocity distribution of the galaxies in each strip (same label as in Figure 2, given in the upper left corner of each panel). The filled blue bins show the galaxies that are considered part of the filament after applying *both* the velocity and edge-separation selection (i.e., within ± 500 km s $^{-1}$ of the central velocities and inside a selected edge-separation range). The red dashed vertical lines in the left panel give the velocity range included in Figure 2, while the blue dashed vertical lines show the range of velocities used to select the galaxies in the filament. The right panels give the distribution of distance to the edge of the strip for galaxies in the velocity range selected for each strip. The filled red histograms indicate galaxies in the proper velocity range, but not in the proper range of edge-separations. For strips A–H the edge of the strip runs along the bottom, from (R.A., decl.) = (223, 41) to (261, 65), while for strips I–P this edge runs from (270, 54) to (218, 64; see Figure 2). The distribution of angular separations from this edge is determined by fitting by a Gaussian if there are 12 or more galaxies, by the first and second moment if there are fewer than 12. The resulting centers are used to define the filament axis; these fits are shown by the solid blue line.

distance of 50 Mpc, which is based on an estimated central velocity of 3500 km s $^{-1}$. These strips overlap by 50%, as shown in Figure 2. The choice of 6 Mpc for the strip width is motivated by the fact that filaments appear to be 2–3 Mpc wide, while the overlapping of the boxes averages out fluctuations.

(2) Next, we make histograms of the velocities of the galaxies in each strip. These are shown on the left side of Figure 3. This makes clear that there is a concentration of galaxies near ~ 3500 km s $^{-1}$, which is especially obvious in strips C through F and J through P. There also is a concentration of galaxies near 6000 km s $^{-1}$ that is seen in boxes A to D and J to M. These are galaxies in a more distant filament that crosses the field. We do not study this filament in detail because our galaxy sample is less complete and at the higher velocities we can not confidently define its boundary. There also are galaxies near 2500 km s $^{-1}$ in boxes A to D, which are due to the 3D properties of the large-scale local structure (i.e., the filament makes a turn). Note that we only consider the galaxies in the blue bins in boxes A to D as part of the filament—most galaxies in the selected velocity range in boxes A and B are not near the filament axis, as can be seen from the righthand panels in Figure 3.

(3) Using the histograms of the velocity distribution, we find the median and rms velocity of all galaxies in the relevant velocity range (selected partly by eye, not using boxes A–C).

Next, we fit the run of the median velocity with the location on the sky to create a linear relation between the position along the filament and velocity. Using the fact that we find the FWHM around the mean to be about 600 km s $^{-1}$, we set a fixed range of 1000 km s $^{-1}$ to select the galaxies. That is, we selected all galaxies in each strip within ± 500 km s $^{-1}$ of the central filament velocity, whose value at each location is determined by a linear fit to the median velocities. The resulting velocity ranges are indicated by the blue filled bins in Figure 3.

(4) With the filament’s velocity structure now constrained, we find the location of the filament axis by deriving the angular separation of each galaxy from the long edge of the guide box (i.e., the outside boundary of the strips shown in Figure 2). This was done for each strip separately, as shown in the righthand panels of Figure 3. We then calculated the centroid and dispersion of this perpendicular distribution (using a Gaussian fit if there are more than 12 galaxies, and a moment calculation if there are fewer). Combining the center of the strip along the long axis with the centroid of the galaxy distribution perpendicular to the axis defines a point on the filament axis. The axis itself is defined by connecting these points, creating 3 Mpc long axis segments.

We note that the lower filament seen in Figure 2 shows a slight velocity gradient, with the central filament velocity increasing from 3300 km s $^{-1}$ in the lower right to 3850 km s $^{-1}$

in the upper left. The upper segment has a much smaller gradient, going from 3750 km s^{-1} on the left to 3550 km s^{-1} on the right. The best single velocity range that includes all galaxies in the filament runs from 2900 to 4300 km s^{-1} , which is the range shown in Figure 2. We note, however, that for our analysis we include the effects of the velocity gradient.

Finally, we note that the filament is mostly parallel to the plane of the sky (which is why it can be easily recognized in a map selecting galaxies in a limited velocity range). The 550 km s^{-1} gradient corresponds to a change in distance of $\sim 8 \text{ Mpc}$, contrasting with a projected length of $\sim 27 \text{ Mpc}$.

3. OBSERVATIONS

3.1. Data sets

To sample the selected galaxy filament shown in Figure 2, we constructed a set of 24 targets. First, we correlated the Véron-Véron QSO catalog with the *GALEX* database, to find all AGN with UV flux larger than $1.5 \times 10^{-15} \text{ erg cm}^{-2} \text{ s}^{-1} \text{ \AA}^{-1}$. This gave a list of 75 objects in the region of interest. We selected most of the brighter ones, but kept a few fainter targets located in strategic directions. The final set of 17 targets were observed using the COS on the *HST* (program 12276), which has a resolution of about 20 km s^{-1} , allowing us to resolve the $\text{Ly}\alpha$ absorbers. That sample is supplemented by seven targets in the same region for which archival data are available; these were mostly obtained using COS, but one case (3C 351.0) was obtained with the *Space Telescope Imaging Spectrograph* (STIS). The STIS data are described by Tripp et al. (2008), and we use the same data set for 3C 351.0. The COS instrument is described in Green et al. (2012) and we use the $\times 1d$ spectra available from the Multimission Archive at Space Telescope, with modifications (see Appendix).

The locations and program information for each target are given in Table 1. The observations in program 12276 were taken with central wavelengths set to 1291 and 1327 Å, resulting in continuous wavelength coverage from ~ 1135 to $\sim 1465 \text{ \AA}$. For six targets, the exposure time is about 2 ks, while for ten targets two orbits were used (giving 5 ks exposures). One target was exposed for three orbits (8.4 ks). When observing for multiple orbits, we also used two different FP-POS settings in the second orbit (central wavelength 1327 Å). The other seven targets were part of eight other programs, using a variety of exposure times and grating settings. The different central wavelengths allow an assessment of detector glitches and fixed-pattern noise, as the same wavelength will fall on two or three different places on the detector. The CALCOS pipeline (v2.19.7) was used to process the raw data, producing one-dimensional extracted spectra.

3.2. AGN Sampling the Filament

Figure 4 shows the directions to the 24 relevant AGN relative to the galaxy filament found in Section 2.2. This figure also shows cases where no $\text{Ly}\alpha$ absorption is found in the velocity range $2900\text{--}4300 \text{ km s}^{-1}$ as open stars and the 10 sightlines with detected $\text{Ly}\alpha$ shown as colored stars. These measurements will be discussed in Section 5.

Table 2 presents the properties of the galaxies near each AGN sightline. It includes all galaxies within the relevant velocity range ($2400\text{--}4800 \text{ km s}^{-1}$, see below) that lie within 1 Mpc of the AGN sightline; if there are fewer than three such

galaxies, it gives the three galaxies with the smallest impact parameter.

For AGN toward which an $\text{Ly}\alpha$ line is seen (see Section 5), Col. 2 shows the velocity of the absorber. Column 4 then gives the difference between that velocity and the filament velocity. For example, 3C 351.0 has an $\text{Ly}\alpha$ line at 3597 km s^{-1} , while the nearest axis segment (at impact parameter 569 kpc) is centered at 3600 km s^{-1} . This implies that the absorption is offset by -3 km s^{-1} from the filament velocity. In the case of galaxies near the sightline, this column also gives the difference between $v(\text{Ly}\alpha)$ and $v(\text{galaxy})$, but only when that difference is less than $\pm 400 \text{ km s}^{-1}$ and either the impact parameter is less than 300 kpc or the ratio of the impact parameter to virial radius (Col. 8) is less than 2. In other words, a non-blank entry in this column for a galaxy row means that in a conventional approach the $\text{Ly}\alpha$ absorption could be associated with the galaxy.

We note that a galaxy’s halo probably does not have a well-defined edge. Gas beyond the virial radius may be falling in if it happens to be moving radially. Other gas beyond the virial radius may be moving mostly transversely and never reach the galaxy. In order to better separate possible halo gas from possible filament gas, we use the arguments by Oort (1970), Maller & Bullock (2004), and Shull (2014). They find that for a Milky Way sized galaxy ($\sim L_*$), the boundary between gas falling in and being part of the IGM is at about 230 kpc. In particular, Shull (2014) discusses the difference between this “accretion radius,” a “gravitational radius,” and the virial radius. The approximation formula given in Section 2.1 gives 140 kpc as the virial radius for an L_* galaxy. Thus a number on the order of $1.5 R_{\text{vir}}$ is justifiable as giving the border between gas in a galaxy halo and gas in the filament.

Using the Shull (2014) approximation shows that there are no $L > 0.05 L_*$ galaxies within these limits that can be associated with the $\text{Ly}\alpha$ detections toward 4C 63.22, FBS 1526+659, H 1821+643, Mrk 486, RBS 1483, RBS 1503, RX J1500.5+5517, and RX J1717.6+6559, so conventionally these would be called void absorbers.

There are galaxies within the 400 km s^{-1} and 300 kpc or $2 R_{\text{vir}}$ limit near the $\text{Ly}\alpha$ absorbers seen toward 3C 351.0, Mrk 290, Mrk 876, RX J1608.3+6814, SBS 1537+577, and SBS 1551+572. However, only toward SBS 1537+577 is the nearest (small) galaxy within 1.5 virial radii located, while for the other sightlines the ratio of the impact parameter to virial radius lies between 1.7 and 2.3 (i.e., these sightlines still pass rather far from the galaxies and do not really sample the CGM of these galaxies).

Thus, using generous standard criteria ($\Delta v < 400 \text{ km s}^{-1}$, $\rho < 300 \text{ kpc}$) at most, four of the thirteen $\text{Ly}\alpha$ absorbers would be associated with a galaxy. Using even more lenient criteria (including galaxies up to two virial radii from the sightline) six of the detections could be associated. Using more physically plausible criteria ($\Delta v < 400 \text{ km s}^{-1}$ and $\rho/R_{\text{vir}} < 1.5$), only one $\text{Ly}\alpha$ absorber samples a galaxy halo. Therefore, basically all $\text{Ly}\alpha$ absorbers in our sample are unlikely to be associated with the halos of galaxies brighter than the SMC ($\sim 0.05 L_*$).

We can estimate how likely it is that our sample of randomly placed sightlines passes inside the virial radius of one of the galaxies. Taking the implied virial radii of all galaxies in our filament and adding up the total sky area that is covered gives a value of 14 Mpc^2 . Because the lower branch of the filament covers about $18^\circ \times 7^\circ$ ($\sim 15.5 \times 6 \text{ Mpc}$), while the upper branch covers about $15^\circ \times 7^\circ$ ($\sim 13 \times 6 \text{ Mpc}$), the total

Table 1
Observations

Target	R.A.	Decl.	z	Program	PI	Obs. ID	Obs. Date	T_{exp} [ks]
(1)	(2)	(3)	(4)	(5)	(6)	(7)	(8)	(9)
3C309.1	14 59 07.6	+71 40 20	0.9050	12486	Bowen	LBP240	2012 03 27	9.4
3C309.1	0.9050	12486	Bowen	LBP245	2012 03 29	9.4
3C351.0	17 04 41.4	+60 44 31	0.3719	8015	Jenkins	O57901	1999 06 27	19.8
3C351.0	0.3719	8015	Jenkins	O57903	1999 06 29	14.4
3C351.0	0.3719	8015	Jenkins	O57902	2000 02 10	18.6
3C351.0	0.3719	8015	Jenkins	O57904	2000 07 25	26.5
4C63.22	15 23 45.9	+63 39 24	0.2040	12276	Wakker	LBI601	2011 08 14	1.9
FBS1526+659	15 27 28.5	+65 48 10	0.3450	12276	Wakker	LBI603	2011 05 02	2.0
H1821+643	18 21 57.2	+64 20 36	0.2970	11484	Hartig	LABO06	2009 07 26	0.6
H1821+643	0.2970	12038	Green	LBGL33	2012 07 06	11.5
Kaz447	17 03 28.9	+61 41 09	0.0773	12276	Wakker	LBI618	2011 10 05	5.2
Mrk290	15 35 52.3	+57 54 09	0.0296	11524	Green	LB4Q02	2009 10 28	3.9
Mrk486	15 36 38.3	+54 33 33	0.0389	12276	Wakker	LBI607	2011 12 18	5.0
Mrk817	14 36 22.1	+58 47 40	0.0315	11505	Noll	LACD01	2009 08 04	2.2
Mrk817	0.0315	11524	Green	LB4Q01	2009 12 28	1.3
Mrk876	16 13 57.2	+65 43 10	0.1290	11686	Arav	LB4F05	2010 04 09	3.1
Mrk876	0.1290	11524	Green	LB4Q03	2010 04 08	9.5
PG1626+554	16 27 56.2	+55 22 32	0.1330	12029	Green	LBGB01	2011 06 15	3.3
RBS1483	15 19 21.6	+59 08 24	0.0781	12276	Wakker	LBI612	2011 06 25	1.9
RBS1503	15 29 07.5	+56 16 06	0.0990	12276	Wakker	LBI614	2010 11 26	2.0
RX J1500.5+5517	15 00 30.8	+55 17 09	0.4048	12276	Wakker	LBI602	2011 05 11	8.4
RX J1503.2+6810	15 03 16.5	+68 10 06	0.1140	12276	Wakker	LBI609	2010 12 31	1.9
RX J1508.8+6814	15 08 52.8	+68 14 07	0.0586	12276	Wakker	LBI608	2010 12 05	1.9
RX J1608.3+6018	16 08 20.5	+60 18 28	0.1780	12276	Wakker	LBI610	2010 11 21	5.2
RX J1717.5+6559	17 17 38.0	+65 59 39	0.2927	12276	Wakker	LBI619	2011 06 22	5.4
SBS1458+535	14 59 49.6	+53 19 09	0.3380	12276	Wakker	LBI611	2011 10 21	5.0
SBS1503+570	15 04 55.6	+56 49 20	0.3589	12276	Wakker	LBI617	2011 10 19	5.2
SBS1521+598	15 21 53.8	+59 40 21	0.2862	12276	Wakker	LBI613	2011 06 12	5.1
SBS1537+577	15 38 10.0	+57 36 13	0.0734	12276	Wakker	LBI606	2011 10 19	5.2
SBS1551+572	15 52 32.7	+57 05 17	0.3660	12276	Wakker	LBI615	2011 03 13	5.1
SBS1624+575	16 25 26.5	+57 27 27	0.0670	12276	Wakker	LBI616	2011 10 17	5.1

filament area is about 170 Mpc^2 . Thus, only about 8% of the filament area is covered by galaxy halos, and only one in twelve $\text{Ly}\alpha$ absorbers should be associated with a galaxy. This is indeed what we find.

As we will now argue, our $\text{Ly}\alpha$ detections are instead likely to be associated with the IGM in the galaxy filament. To quantify the relation between detections and the filament, we define a new quantity: the ‘‘filament impact parameter’’ ($\rho(\text{fil})$) as the separation between an AGN sightline and the nearest axis segment. This is the product of the angular separation scaled by the distance corresponding to the segment’s recession velocity (i.e., the central velocity of each filament strip, found in the manner described previously). The resulting impact parameters are given in Col. 4 Table 2 under the entry ‘‘Filament Axis’’ after each AGN’s name.

4. SIMULATIONS

4.1. Description

In order to interpret the observations, we analyzed the cosmological hydrodynamical simulations of Oppenheimer et al. (2010). In this section we first describe these simulations and the information that we extracted from them, so that we can refer to this in the results section. The simulations are *Gadget-2* smoothed particle hydrodynamic simulations run with 384^3 gas and dark matter particles in a random periodic volume of $48 h^{-1} \text{ Mpc}$. The cosmology used is $\Omega_M = 0.28$, $\Omega_\Lambda = 0.78$, $H_0 = 70 \text{ km s}^{-1} \text{ Mpc}^{-1}$, $\Omega_b = 0.046$, $n = 0.96$, and $\sigma_8 = 0.82$.

The gravitational softening length is $2.5 h^{-1} \text{ kpc}$ and the gas-mass resolution is $3.5 \times 10^7 M_\odot$, both of which are sufficient to resolve the structure of the $\text{Ly}\alpha$ forest. Davé et al. (2010) used a series of these simulations with different feedback models to model the $\text{Ly}\alpha$ forest statistics, and checked that the $\text{Ly}\alpha$ forest statistics are resolution converged by using a $96 h^{-1} \text{ Mpc}$ box with $3.375\times$ lower resolution. We use the ‘‘vzw’’ simulation, because its galaxy mass function shown in Oppenheimer et al. (2010) is most similar to the observed galaxy mass function of Bell et al. (2003), which used 2MASS K_s -band magnitudes along with SDSS magnitudes. This simulation mimics momentum-driven winds from starbursts as described in Oppenheimer & Davé (2008). However, the other models described in that paper give very similar results.

We use Spline Kernel Interpolative Denmax (SKID; <http://www-hpcc.astro.washington.edu/tools/skid.html>) to identify galaxies (Kereš et al. 2005; Oppenheimer et al. 2010). We determine the broadband photometric properties of each galaxy by summing up the single stellar population models of Bruzual & Charlot (2003) within each star particle, for which we have an age and metallicity, assuming a Chabrier (2003) initial mass function, and adding a dust correction based on the galaxy’s metallicity as explained in Finlator et al. (2006).

4.2. Finding Filaments in the Simulations

To compare these simulations with the observations we take a different approach than usual. Usually, simulations are displayed by taking a 3D cube and collapsing a slice onto a side

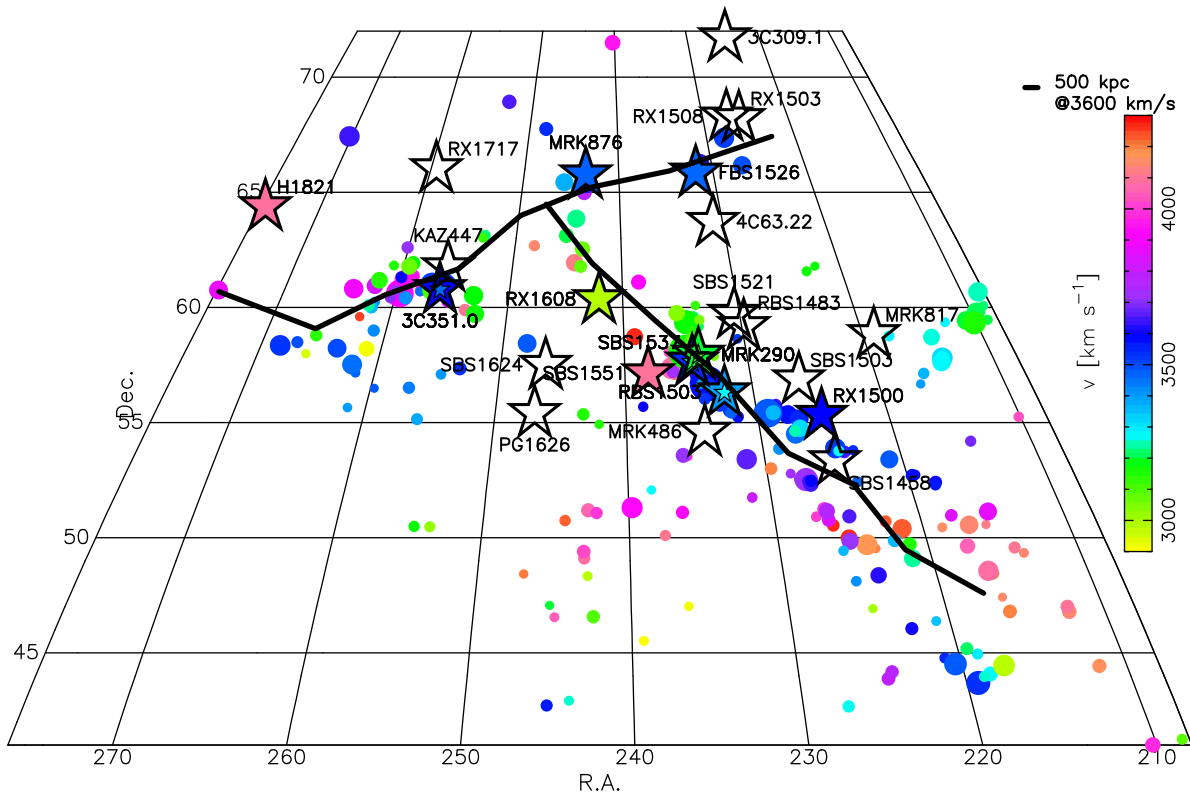


Figure 4. Distribution of galaxies (colored circles) and AGN (open and colored stars) in the galaxy filament. Only galaxies with velocities between 2900 and 4300 km s^{-1} are shown. The sizes of the galaxy circles are proportional to the square of their diameters (i.e., area), while the color indicates their velocities, following the scale bar on the right. AGN toward which Ly α absorption is seen are shown by filled colored stars, while non-detections are indicated by open stars. The axes of the two filament segments are shown by the wiggly black lines. See the text for the derivation of these axes.

of the cube. Here, however, we take the simulations and project the galaxies and H I volume density onto the sky, taking into account the fact that a sky pixel represents a cone through the simulation cube, not a rectangular bar. We identify simulated filaments that look like the observed filament, based on how the galaxies appear in the simulated skies from various locations chosen within the simulation, which we call “viewpoints.”

To find viewpoints, we started with the SKID-identified galaxies, projecting their locations onto the same region of the sky as our observed filament ($\sim 30^\circ \times 30^\circ$ centered on R. A. = 240° , decl. = 55°). We then calculated each galaxy’s apparent velocity, combining its Hubble flow velocity with its peculiar velocity and selected the galaxies in a 1400 km s^{-1} wide window between 2900 and 4300 km s^{-1} . Stepping through the simulation cube in 2 Mpc intervals in x , y , and z (i.e., 32 steps each) and plotting the resulting distribution of simulated galaxies on the sky, we found the viewpoints where a galaxy filament stood out visually. Next, we refined the search around each of these viewpoints to get the best viewpoint to within 1 Mpc. Using the galaxy distances and simulated K_s magnitudes, we find apparent magnitudes. Applying a magnitude cut of $K_s < 19$ and using just the galaxy locations, we derive filament axes for each viewpoint, using the same method as was used for the observations.

Figure 5 presents the galaxy distribution for one viewpoint, in order to show that the visual impression given by the simulation is similar to that given by the data. To determine how well the simulated galaxy filaments represent our observed galaxy filament, we compare the galaxy density along the filament and the K_s -band luminosity function (Figure 6), using

the boxes around the filaments seen in Figure 7. These have lengths of 18–22 Mpc. Within these boxes we find 336, 157, 156, and 127 galaxies with $K_s < 19$ for filaments a, b, c, and d, respectively. The lower branch of our observed filament has 137 galaxies and a length of 20.9 Mpc (i.e., similar to the simulated filaments).

When comparing simulated and observed filament galaxy statistics, we apply a luminosity cut of $K_s = -16.3$, which corresponds to $M_* = 10^9 M_\odot$ and is the quoted simulation resolution limit. Even though the vzw simulation does not quench galaxies as required by observations, this does not matter, because Oppenheimer et al. (2010) show that the number density of galaxies above $10^{9.0} M_\odot$ is in agreement with Bell et al. (2003) within a factor of 30% (see their Figure 6). While we did explore other wind models including a no wind model and a constant wind model, there is statistically no difference in filament statistics for a given ionization background.

Figure 6 shows the galaxy filament density as a function of impact parameter for the luminosity cut. Even though more galaxies were used to identify the observed filament and make the initial identification of simulated filaments, we plot the galaxy densities with absolute $K_s < -16.3$ binned into 500 kpc bins perpendicular to the filament in areal density units. The observed filament has a total density of $2.6 \text{ galaxies Mpc}^{-1}$ within 5 Mpc, while simulated filaments (a), (b), (c), and (d) have 3.8, 2.0, 1.9, and 1.7, thus bracketing the observed filament density. Based on binned areal density, no filament exactly matches the observed filament, but filament (a) is generally denser, and filaments (b), (c), and (d) are less dense

Table 2
Galaxies Between 2400 and 4800 km s⁻¹ within 1 Mpc of Each Sightline

Target	Galaxy	cz (km s ⁻¹)	Δv (km s ⁻¹)	ρ (kpc)	Diameter (kpc)	L/L_*	R_{vir}	ρ/R_{vir}	Type
(1)	(2)	(3)	(4)	(5)	(6)	(7)	(8)	(9)	(10)
3C309.1	Filament Axis	3600	...	3908
3C309.1	IC1110	3373	...	3854	24.6	0.86	158	24.3	Sa
3C309.1	UGC09734	3341	...	4756	19.9	0.55	137	34.7	Sm
3C309.1	CGCG338-038	3827	...	4737	15.9	0.34	117	40.3	...
3C351.0	Ly α @ 3597,3459
3C351.0	Filament Axis	3600	-3, -141	569
3C351.0	Mrk0892	3617	-20, -158	179	12.9	0.22	101	1.8	Pair
3C351.0	NGC6307	3057	...	284	22.7	0.72	149	1.9	PSBS0P.
3C351.0	NGC6306	2973	...	271	19.3	0.51	134	2.0	.SBS2P*
3C351.0	NGC6310	3419	...	406	34.5	1.76	200	2.0	.S.3*
3C351.0	NGC6292	3411	...	375	22.4	0.70	148	2.5	.S.4..
3C351.0	SDSSJ170327.95+610631.5	3313	...	333	9.2	0.11	81	4.1	...
3C351.0	2MASXJ17071270+6055144	3099	360	280	3.6	0.01	42	6.5	H II
3C351.0	SBS1700+603	3736	...	616	9.6	0.12	83	7.4	...
3C351.0	SDSSJ171138.94+604341.8	3855	...	828	8.3	0.08	75	11.0	...
3C351.0	SDSSJ171140.34+604115.6	3350	...	727	5.5	0.04	57	12.7	...
3C351.0	UGC10745	3059	...	700	2.7	0.01	35	19.8	Sdm
4C63.22	Ly α @ 2420
4C63.22	Filament Axis	3600	-1180	2333
4C63.22	KHG1-C07	2548	...	2413	1.0	0.00	3	679.2	...
4C63.22	SBS1543+593	2698	...	3564	1.0	0.00	3	1003.3	dwarf
4C63.22	KHG1-C09	2848	...	3593	1.0	0.00	3	1011.5	Comp
FBS1526+659	Ly α @ 3476
FBS1526+659	Filament Axis	3600	-124	369
FBS1526+659	KHG1-C07	2548	...	3693	1.0	0.00	3	1039.8	...
FBS1526+659	KHG1-C09	2848	...	4593	1.0	0.00	3	1293.1	Comp
FBS1526+659	SBS1543+593	2698	...	4821	1.0	0.00	3	1357.3	dwarf
H1821+643	Ly α @ 2825,4087
H1821+643	Filament Axis	3600	-775, 487	3249
H1821+643	NGC6636NED01	4393	...	2491	40.2	2.4	222	11.2	.S?....
H1821+643	NGC6687	3374	...	4239	28.6	1.18	175	24.1	SAd
H1821+643	NGC6701	3965	...	4369	29.6	1.27	180	24.3	PSBS1..
Kaz447	Filament Axis	3600	...	184
Kaz447	NGC6310	3419	...	762	34.5	1.76	200	3.8	.S.3*
Kaz447	NGC6292	3411	...	669	22.4	0.70	148	4.5	.S.4..
Kaz447	NGC6307	3057	...	826	22.7	0.72	149	5.5	PSBS0P.
Kaz447	SDSSJ170327.95+610631.5	3313	...	485	9.2	0.11	81	6.0	...
Kaz447	NGC6306	2973	...	817	19.3	0.51	134	6.1	.SBS2P*
Kaz447	Mrk0892	3617	...	949	12.9	0.22	101	9.3	Pair
Kaz447	2MASXJ17071270+6055144	3099	...	699	3.6	0.01	42	16.3	H II
Kaz447	UGC10745	3059	...	673	2.7	0.01	35	19.0	Sdm
Mrk290	Ly α @ 3089
Mrk290	Filament Axis	3600	-511	97
Mrk290	NGC5987	3010	79	475	46.4	3.3	245	1.9	.S.3..
Mrk290	2MASXJ15351422+5730529	3092	...	318	8.5	0.09	76	4.1	H II
Mrk290	SDSSJ153802.75+573018.3	3525	...	446	10.4	0.14	87	5.1	Sd(f)
Mrk290	CGCG297-017	3282	...	506	10.4	0.14	87	5.8	...
Mrk290	SDSSJ153733.00+583447.8	2932	...	542	10.7	0.15	89	6.0	Sc(f)
Mrk290	SBS1533+574A	3348	...	566	6.8	0.06	66	8.6	H II
Mrk290	SDSSJ153040.88+575301.0	2896	...	519	5.7	0.04	58	8.9	...
Mrk290	SDSSJ153742.05+570506.4	3469	...	762	7.2	0.06	68	11.2	...
Mrk290	SBS1540+576	3717	...	760	6.7	0.05	65	11.7	...
Mrk290	SDSSJ153706.68+585651.5	2989	...	819	6.6	0.05	64	12.6	...
Mrk290	SBS1533+574B	3429	...	579	3.9	0.02	44	12.9	H II
Mrk290	2MASXJ15335796+5650509	3260	...	915	3.6	0.01	42	21.5	...
Mrk290	SDSSJ152956.69+582635.9	2908	...	718	2.5	0.01	33	21.7	...
Mrk486	Ly α @ 4386
Mrk486	Filament Axis	3600	786	1910

Table 2
(Continued)

Target	Galaxy	cz (km s^{-1})	Δv (km s^{-1})	ρ (kpc)	Diameter (kpc)	L/L_*	R_{vir}	ρ/R_{vir}	Type
(1)	(2)	(3)	(4)	(5)	(6)	(7)	(8)	(9)	(10)
Mrk486	SBS1543+593	2698	...	3342	1.0	0.00	3	940.8	dwarf
Mrk486	KHG1-C07	2548	...	3841	1.0	0.00	3	1081.3	...
Mrk486	KHG1-C09	2848	...	4615	1.0	0.00	3	1299.3	Comp
Mrk817	Filament Axis	3650	...	6208
Mrk817	[DYC2005]443	2998	...	4679	1.0	0.00	3	1317.4	Blue
Mrk817	RCS06100303673	3298	...	4717	1.0	0.00	3	1327.9	...
Mrk817	RCS06100304426	3298	...	4742	1.0	0.00	3	1335.1	...
Mrk876	$\text{Ly}\alpha$ @ 3476
Mrk876	Filament Axis	3600	-124	540
Mrk876	UGC10294	3504	-28	274	25.6	0.93	162	1.7	Sm?
Mrk876	UGC10376	3246	...	797	19.3	0.51	134	5.9	Sm:
Mrk876	NGC6135	3644	...	685	13.9	0.25	107	6.4	...
PG1626+554	Filament Axis	3550	...	5684
PG1626+554	NGC6258	3064	...	4753	22.4	0.70	148	31.9	E.....
PG1626+554	KHG1-C09	2848	...	4912	1.0	0.00	3	1383.0	Comp
PG1626+554	SBS1543+593	2698	...	4919	1.0	0.00	3	1384.9	dwarf
RBS1483	$\text{Ly}\alpha$ @ 2726
RBS1483	Filament Axis	3600	-874	2260
RBS1483	NGC5894	2466	...	839	33.6	1.66	196	4.3	.SB.8?.
RBS1483	SDSSJ151827.06+582658.6	2555	...	469	7.8	0.07	72	6.5	...
RBS1483	Mrk0847	2540	...	658	10.2	0.13	86	7.6	.S?....
RBS1483	SDSSJ152209.95+583819.5	3349	...	535	5.8	0.04	59	9.0	...
RBS1483	UGC09837	2657	...	880	7.3	0.06	69	12.7	SAB(s)c
RBS1483	SDSSJ151917.62+603435.9	2535	...	953	4.8	0.03	51	18.4	...
RBS1503	$\text{Ly}\alpha$ @ 3269, 3306
RBS1503	Filament Axis	3600	-331, -294	306
RBS1503	NGC5965	3412	...	677	55.6	4.9	277	2.4	.S..3..
RBS1503	Mrk0482	3357	...	640	13.2	0.23	103	6.2
RBS1503	CGCG274-047	3355	...	517	9.3	0.11	81	6.3	...
RBS1503	2MASXJ15332453+5636315	3553	...	624	10.2	0.13	86	7.2	...
RBS1503	Mrk0481	3298	...	726	8.9	0.10	78	9.2	E
RBS1503	MCG+09-26-001	3366	...	793	9.1	0.10	80	9.9	...
RBS1503	SDSSJ153325.63+564156.5	3362	...	636	6.1	0.04	61	10.4	...
RBS1503	SDSSJ153007.14+553432.8	3356	...	612	5.1	0.03	54	11.3	...
RBS1503	SBS1524+554	3409	...	978	8.5	0.09	76	12.8	BlueCG
RBS1503	SDSSJ153558.83+564108.2	3213	...	859	6.1	0.04	61	14.0	BLAGN
RBS1503	2MASXJ15335796+5650509	3260	...	744	3.6	0.01	42	17.5	...
RX J1500.5+5517	$\text{Ly}\alpha$ @ 3592
RX J1500.5+5517	Filament Axis	3650	-58	2031
RX J1500.5+5517	UGC09737	3367	...	911	16.1	0.35	118	7.7	S
RX J1500.5+5517	SDSSJ150621.06+550842.1	3374	...	738	7.7	0.07	71	10.3	...
RX J1500.5+5517	SDSSJ150804.21+551954.0	3400	...	948	7.4	0.07	69	13.6	...
RX J1500.5+5517	SDSSJ150654.40+553218.2	3295	...	805	4.8	0.03	51	15.5	...
RX J1500.5+5517	SDSSJ145718.28+543105.9	3216	...	750	2.8	0.01	36	20.7	...
RX J1503.2+6810	Filament Axis	3600	...	1016
RX J1503.2+6810	IC1110	3373	...	1003	24.6	0.86	158	6.3	Sa
RX J1503.2+6810	UGC09855	3480	...	2538	22.2	0.69	147	17.2	Im:
RX J1503.2+6810	CGCG297-009	2500	...	4633	1.0	0.00	3	1304.4	Sd(f)
RX J1508.8+6814	Filament Axis	3600	...	1202
RX J1508.8+6814	IC1110	3373	...	799	24.6	0.86	158	5.0	Sa
RX J1508.8+6814	UGC09855	3480	...	2249	22.2	0.69	147	15.2	Im:
RX J1508.8+6814	CGCG297-009	2500	...	4624	1.0	0.00	3	1301.9	Sd(f)
RX J1608.3+6018	$\text{Ly}\alpha$ @ 2983, 2886
RX J1608.3+6018	Filament Axis	3550	-567, -664	880
RX J1608.3+6018	UGC10247	2995	-12, -109	199	14.3	0.27	109	1.8	SBm:
RX J1608.3+6018	UGC10279NED01	4421	...	563	14.1	0.26	108	5.2	Sb

Table 2
(Continued)

Target	Galaxy	cz (km s^{-1})	Δv (km s^{-1})	ρ (kpc)	Diameter (kpc)	L/L_*	R_{vir}	ρ/R_{vir}	Type
(1)	(2)	(3)	(4)	(5)	(6)	(7)	(8)	(9)	(10)
RX J1608.3+6018	UGC10279NED02	4429	...	566	13.1	0.22	102	5.5	SBC
RX J1608.3+6018	KHG1-C10	4317	...	814	1.0	0.00	3	229.2	...
RX J1717.5+6559	Ly α @4705
RX J1717.5+6559	Filament Axis	3600	1105	4330
RX J1717.5+6559	NGC6310	3419	...	4436	34.5	1.76	200	22.2	.S.3*
RX J1717.5+6559	HIJASSJ1720+71	2495	...	3526	1.0	0.00	3	992.8	...
RX J1717.5+6559	SSTXFLSJ171614.7+602439	3298	...	4669	1.0	0.00	3	1314.4	...
SBS1458+535	Filament Axis	3650	...	563
SBS1458+535	NGC5820	3335	...	514	24.6	0.86	158	3.2	.L....
SBS1458+535	UGC09663	2420	...	498	18.5	0.47	130	3.8	Im:
SBS1458+535	NGC5821	3376	...	540	19.1	0.50	133	4.0	S?
SBS1458+535	SDSSJ145753.64+534602.5	3080	...	428	7.2	0.06	68	6.2	...
SBS1458+535	SDSSJ145620.69+534336.8	3458	...	591	10.1	0.13	86	6.9	...
SBS1458+535	UGC09632	3206	...	454	4.9	0.03	53	8.6	.SA.7..
SBS1458+535	SBS1452+540	3351	...	903	6.7	0.05	64	13.9	E
SBS1503+570	Filament Axis	3600	...	2395
SBS1503+570	CGCG297-009	2500	...	2993	1.0	0.00	3	842.6	Sd(f)
SBS1503+570	KHG1-C07	2548	...	3578	1.0	0.00	3	1007.2	...
SBS1503+570	SBS1543+593	2698	...	4020	1.0	0.00	3	1131.7	dwarf
SBS1521+598	Filament Axis	3600	...	2390
SBS1521+598	NGC5894	2466	...	919	33.6	1.66	196	4.7	.SB.8?.
SBS1521+598	SDSSJ151827.06+582658.6	2555	...	871	7.8	0.07	72	12.1	...
SBS1521+598	SDSSJ151917.62+603435.9	2535	...	637	4.8	0.03	51	12.3	...
SBS1521+598	SDSSJ152209.95+583819.5	3349	...	894	5.8	0.04	59	15.0	...
SBS1537+577	Ly α @ 3541, 3257
SBS1537+577	Filament Axis	3600	-59, -343	293
SBS1537+577	SDSSJ153802.75+573018.3	3525	16, -268	91	10.4	0.14	87	1.0	Sd(f)
SBS1537+577	NGC5987	3010	247	444	46.4	3.3	245	1.8	.S..3..
SBS1537+577	NGC5965	3412	...	914	55.6	4.9	277	3.3	.S..3..
SBS1537+577	2MASXJ15351422+5730529	3092	...	322	8.5	0.09	76	4.2	H II
SBS1537+577	CGCG297-017	3282	...	521	10.4	0.14	87	5.9	...
SBS1537+577	SBS1540+576	3717	...	389	6.7	0.05	65	6.0	...
SBS1537+577	UGC10002	4052	...	875	20.7	0.59	140	6.2	SB?
SBS1537+577	SDSSJ153742.05+570506.4	3469	...	466	7.2	0.06	68	6.8	...
SBS1537+577	SBS1533+574A	3348	...	534	6.8	0.06	66	8.1	H II
SBS1537+577	SDSSJ153733.00+583447.8	2932	...	745	10.7	0.15	89	8.3	Sc(f)
SBS1537+577	MCG+10-22-037	3969	...	992	15.7	0.33	116	8.5	Scd(f)
SBS1537+577	SDSSJ154434.41+571243.8	3568	...	868	10.8	0.15	90	9.6	...
SBS1537+577	SDSSJ154331.89+571434.0	3975	...	821	7.1	0.06	67	12.1	...
SBS1537+577	SBS1533+574B	3429	...	546	3.9	0.02	44	12.2	H II
SBS1537+577	SDSSJ153558.83+564108.2	3213	...	801	6.1	0.04	61	13.1	BLAGN
SBS1537+577	SDSSJ153040.88+575301.0	2896	...	780	5.7	0.04	58	13.4	...
SBS1537+577	SBS1542+573C	4027	...	885	5.8	0.04	58	15.1	...
SBS1537+577	SDSSJ153325.63+564156.5	3362	...	962	6.1	0.04	61	15.8	...
SBS1537+577	SDSSJ154054.24+565139.2	3408	...	728	3.3	0.01	40	18.0	Irr(sa)
SBS1537+577	2MASXJ15335796+5650509	3260	...	797	3.6	0.01	42	18.7	...
SBS1551+572	Ly α @ 4097
SBS1551+572	Filament Axis	3600	497	1778
SBS1551+572	SDSSJ155235.47+565604.2	4104	-7	161	7.3	0.06	69	2.3	...
SBS1551+572	SBS1553+573	3610	...	290	9.6	0.12	83	3.5	E
SBS1551+572	SDSSJ154434.41+571243.8	3568	...	997	10.8	0.15	90	11.0	...
SBS1624+575	Filament Axis	3550	...	4103
SBS1624+575	KHG1-C09	2848	...	3635	1.0	0.00	3	1023.4	Comp
SBS1624+575	SBS1543+593	2698	...	3973	1.0	0.00	3	1118.6	dwarf
SBS1624+575	KHG1-C10	4317	...	4084	1.0	0.00	3	1149.7	...

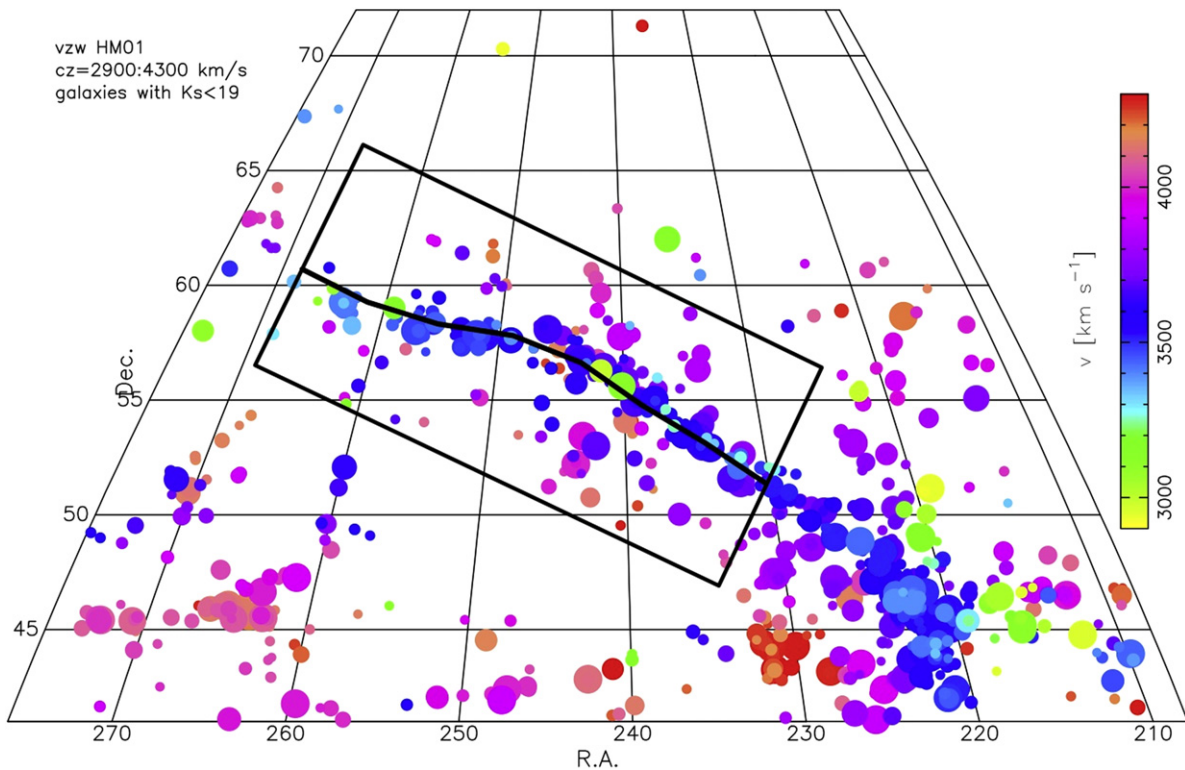


Figure 5. View of the galaxies as seen from one viewpoint in the vzw simulation. Galaxies are shown by colored circles, with the same scalings as used for Figures 2 and 4. The filament axis is shown as a thick black line, found by treating the simulated galaxies in the same manner as the observations. Finally, a rectangular outline box shows the area of the simulated sky used to measure $N(\text{H I})$ as a function of filament impact parameter.

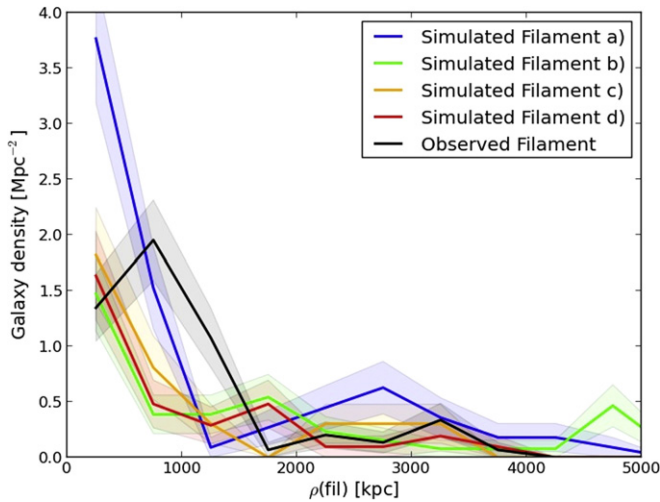


Figure 6. Density of galaxies brighter than absolute $K_s = -16.3$ as a function of the filament impact parameter for each of the four simulated viewpoints (colors) and the observations (black). All galaxies out to 5 Mpc from the filament axis are included and binned every 0.5 Mpc. The vertical scale gives the number of galaxies per square Mpc in each bin.

within 1.5 Mpc and have similar areal densities as the observations out to 4 Mpc. We also checked the galaxy luminosity functions along the filaments and found that the simulated luminosity functions are shaped like we expect from Oppenheimer et al. (2010). They have a similar density of galaxies, but more bright galaxies than the observations.

4.3. Ionizing Radiation in the Simulations

To calculate an H I column density map as seen from the selected viewpoints, we used four different levels for the intensity of the EGB radiation. First, we took the model of Haardt & Madau (2001; HM01), in which the contribution of galaxies and quasars to the ionizing flux is comparable at all redshifts. Second, we used the purportedly improved model of Haardt & Madau (2012; HM12), which used more observational constraints. In this version, the escape fraction of ionizing radiation from galaxies evolves over time, such that the contribution of galaxies at $z \sim 0$ is minimal. As Kollmeier et al. (2014) show, the predicted H I column density distribution at $z = 0$ then fails to match the distribution observed by Danforth et al. (2014), giving five times too many H I clouds at any given column density. The HM01 version of the radiation field matches the observations better. Kollmeier et al. (2014) discuss the possible causes and remedies to improve the match between the observed $z \sim 0$ Ly α column density distribution and the distribution implied by the HM12 model, but are unable to come to a conclusion. Shull et al. (2015) propose to solve the discrepancy by using a different simulation, which has stronger heating, and then a higher escape fraction (5%) of ionizing photons from star-forming galaxies gives a factor two more ionizing photons. Khaire & Srianand (2015), however, redo the modeling of the EGB from scratch and suggest that the QSO luminosity function alone implies a factor two more ionizing photons than found by HM12, which combined with a 4% escape fraction resolves the discrepancy. In Sections 5.3 and 5.5 we describe our new way of constraining the EGB models, now based on the spatial

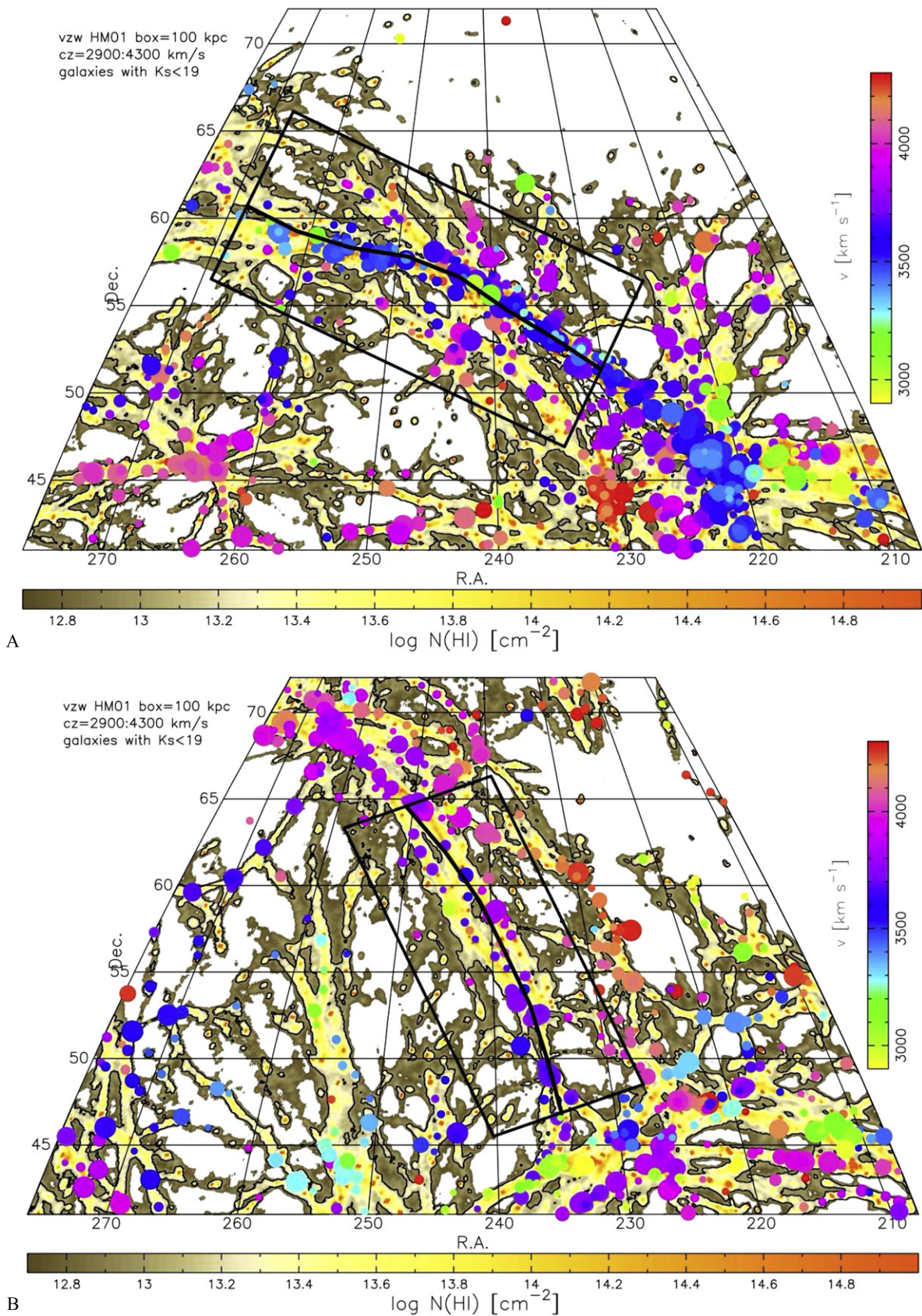


Figure 7. (a) View of the vzw simulation (with 100 kpc voxels) from four different viewpoints in the cube. HI column densities calculated using the Haardt & Madau (2001) extragalactic background radiation field are shown by the gray–yellow–red colors, with a contour at $\log N(\text{HI}) = 13$, which is our detection limit. Galaxies are shown by colored circles, with the same scalings as used for Figures 2, 4, and 5. The filament axis is shown as a thick black line, found by treating the simulated galaxies in the same manner as the observations. A rectangular outline box shows the area of simulated sky used to measure $N(\text{HI})$ as a function of filament impact parameter.

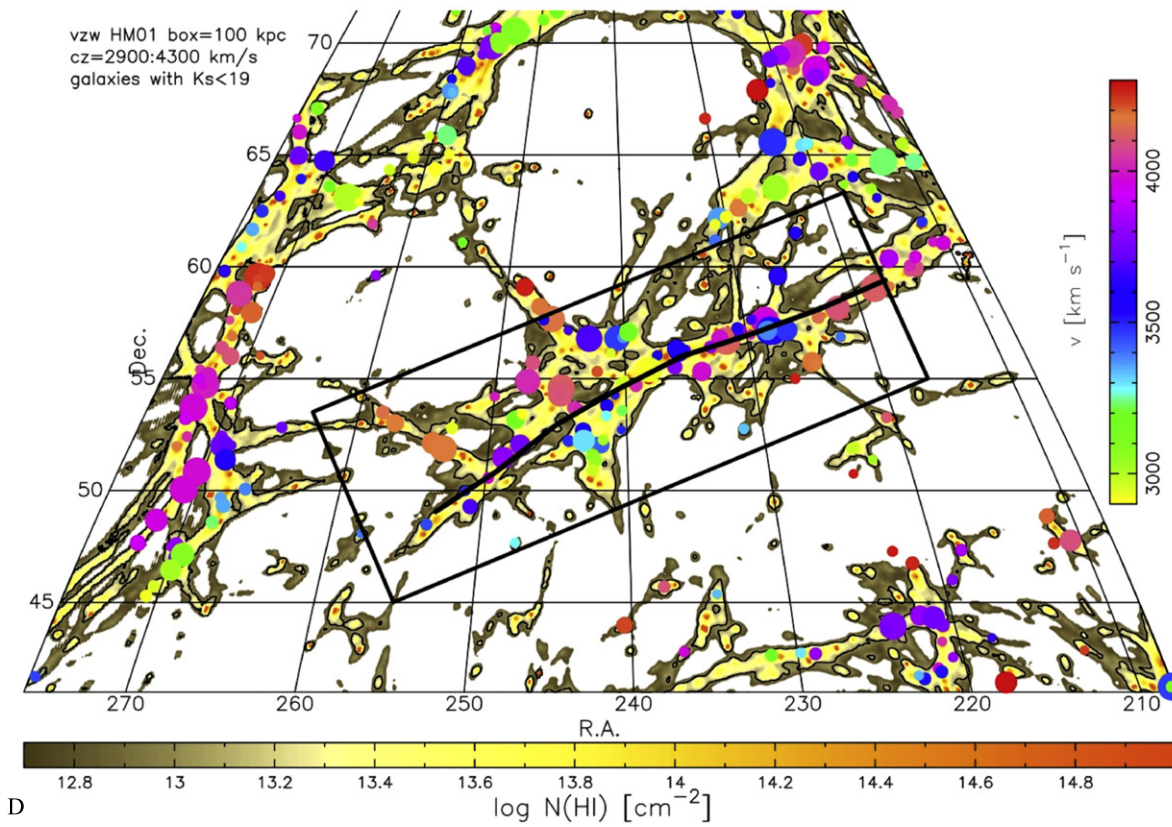
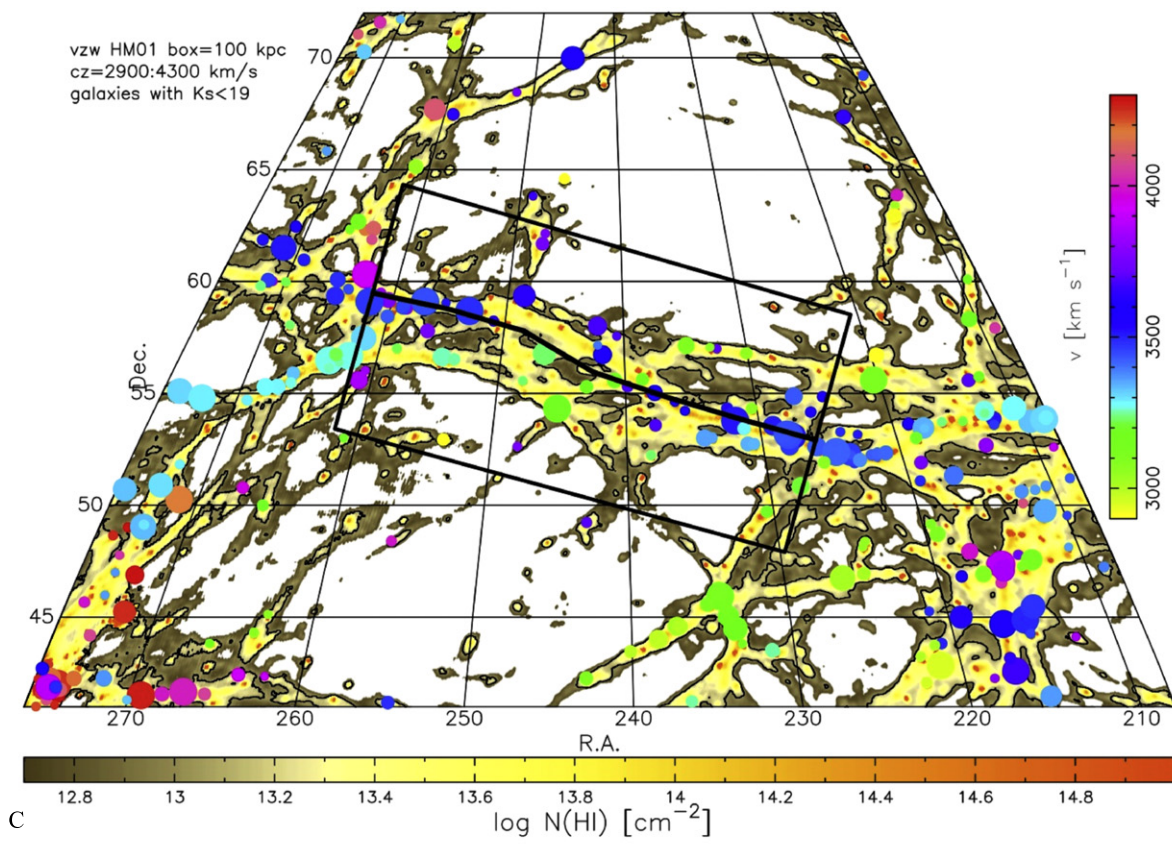


Figure 7. (Continued.)

distribution of the Ly α forest in relation to galaxy filaments, rather than using the column density distribution.

We now describe our method to calculate H I column densities, which depend on the assumed intensity of ionizing radiation. Our method produces a more realistic description of the observations than the standard method of collapsing a simulation cube onto one of the side planes. We start by calculating the distance to each (3D) simulation voxel (i.e., a 100×100 kpc grid cell), given a viewpoint. This is converted to its Hubble flow velocity, using a Hubble constant of $71 \text{ km s}^{-1} \text{ Mpc}^{-1}$. To this recession velocity we add the peculiar velocity of the material in that simulation voxel to get its apparent velocity. Selecting a range of velocities, we then draw a diverging bundle of sightlines through the cube for each individual sky pixel, with the sightlines in a bundle close enough that several span the most distant voxel used. Sampling each sightline in steps of about $1/3$ the size of a voxel, we sum the H I volume density that was calculated using the value of the total gas density in that voxel, combined with the model for the EGB. This is multiplied by the pathlength to find the column density in each sky pixel. Although we use SPH simulations, we transform the particles onto a 3D grid with 100 kpc cells, which corresponds to $6/5$ at redshifts of 3500 km s^{-1} . We also tried using 50 kpc cells, and found no statistical difference, which is to be expected because structures in the Ly α forest structures are larger than this (Davé et al. 2010).

The resulting H I column densities are shown in Figure 7. From these figures, it is clear that with a velocity range of $\sim 1400 \text{ km s}^{-1}$ a single filament as seen in the distribution of galaxies is obvious, but in the H I column density distribution other filaments “spill over” into the selected velocity range. Figures 8(a)–(d) show the effect of varying the intensity of the ionizing background on the H I column density maps.

4.4. Properties of the Gas in the Simulation

To conclude this discussion of the simulations, we present some of the characteristics of the neutral hydrogen. In Figure 9 we show the relation between the total and neutral amounts of hydrogen for the pixels inside the selection box in the first filament (see Figure 7(a)), using the HM01 EGB model. The left panel shows that within the about 8 Mpc wide strip along the filament, the total hydrogen column density (integrated from $cz = 2900$ to 4300 km s^{-1}) only varies from about $\log N(\text{H}) = 18.5$ to 20.0 . The concentration of dots on the right is caused by sightlines with high $N(\text{H I})$, which occur in voxels that contain a galaxy. Panel (b) reveals that the ratio of total to neutral hydrogen (i.e., the ionization correction) ranges from about $10^{+6.5}$ for absorbers with $\log N(\text{H I}) \sim 13$ to about 10^{+1} when $\log N(\text{H I}) \sim 19.5$, with a spread of only about 1 dex at any given value of $N(\text{H I})$. This plot clearly shows that (a) the H I column density can serve as a proxy for the total hydrogen column density and (b) the H I traces only a very small fraction of the baryons, which was demonstrated by Davé et al. (1999), although they did not explicitly show this in a figure.

The top and middle histograms in Figure 10 show the number of pixels and the total or neutral hydrogen mass as a function of the total and neutral hydrogen volume density, for the pixels inside the outlined box for the first viewpoint (see Figure 7(a)). The vertical line in the left panels represents the average hydrogen density of the universe: $n(\text{H}) = 0.75 \times 0.046$

$(3 \text{ H}_2)/(8\pi\text{G}) = 10^{-6.7} \text{ cm}^{-3}$. The bottom histograms give the cumulative mass fraction as function of volume density. Three different curves are shown, with the black curve including all 100 kpc^3 simulation voxels included inside the box outlined in Figure 7(a) and the blue curve showing the voxels in which a simulated galaxy is present. The red curve is for the 27 voxels containing each galaxy (not double counting cases where these overlap when there are multiple galaxies in the list that are close together; i.e., they represent the CGM out to about 150 kpc).

This figure shows that in a given random direction through the filament, most voxels have low volume density. As expected, the circumgalactic and galactic voxels have the highest average densities ($\sim 10^{-3}$ baryons per cm^3 in a $300 \times 300 \times 300 \text{ kpc}$ cube). The middle left panel shows that the baryon mass is fairly evenly distributed between all volume densities. In the 0.1 dex bins near $\log n(\text{H}) = -8, -7, -6, -5, -4,$ and -3 , there are 1, 3, 6, 5, 4, and 1×10^{12} solar masses of baryons, respectively. Thus, the total mass of baryons is dominated by the extended IGM. In contrast, the distribution of neutral hydrogen mass is dominated by the voxels around galaxies (see right middle panel).

5. RESULTS

5.1. Spectral Analysis

We now describe the results we derive from the data and the comparison with simulations.

We applied our wavelength-correction and error calculation code to all the spectra listed in Table 1 and then identified the absorption lines in each, making sure to identify each feature between 1216 and 1240 Å (i.e., 0 to 6000 km s^{-1} relative to Ly α). Figure 11 shows the relevant section of each spectrum, including a continuum that was determined by fitting a low-order (1st or 2nd) polynomial to line-free regions near the window shown. The targets are sorted by filament impact parameter (given in the bottom right corner of each panel). It is obvious that absorption is present close to the filament (left column) and absent far from the filament (right column).

Since most of our targets have relatively low redshift ($z < 0.4$), there are few hard-to-identify lines and most features seen are clearly Ly α or metal lines associated with a higher redshift system. In fact, there are only a handful of non-Ly α lines that fall in the window of interest for this paper: Ly ϵ at $z = 0.316$ toward 3C 351.0, Ly δ at $z = 0.297$ toward H 1821 +643, Ly μ –Ly ρ in a Lyman limit system at $z = 0.347$ toward RX J1500.5+5517, and C II $\lambda\lambda 903.6, 903.9$ in a Lyman limit system at $z = 0.367$ toward SBS 1551+572. These lines are labeled in Figure 11. All other visible features are identified as Ly α .

We used two different methods to measure the column densities and linewidths in the Ly α lines, using the same continuum fits. First, we calculated column density using the apparent optical depth method (see Savage & Sembach 1991):

$$N = \int N_a(v) dv = \int \frac{m_e c}{\pi e^2} f \lambda \ln \frac{C(v)}{F(v)},$$

with $F(v)$ the observed profile, $C(v)$ the fitted continuum, f the oscillator strength (0.4164 for Ly α), and λ the rest wavelength (1215.67 Å). We also calculated the second moment of the apparent optical depth profile to derive a linewidth. We then

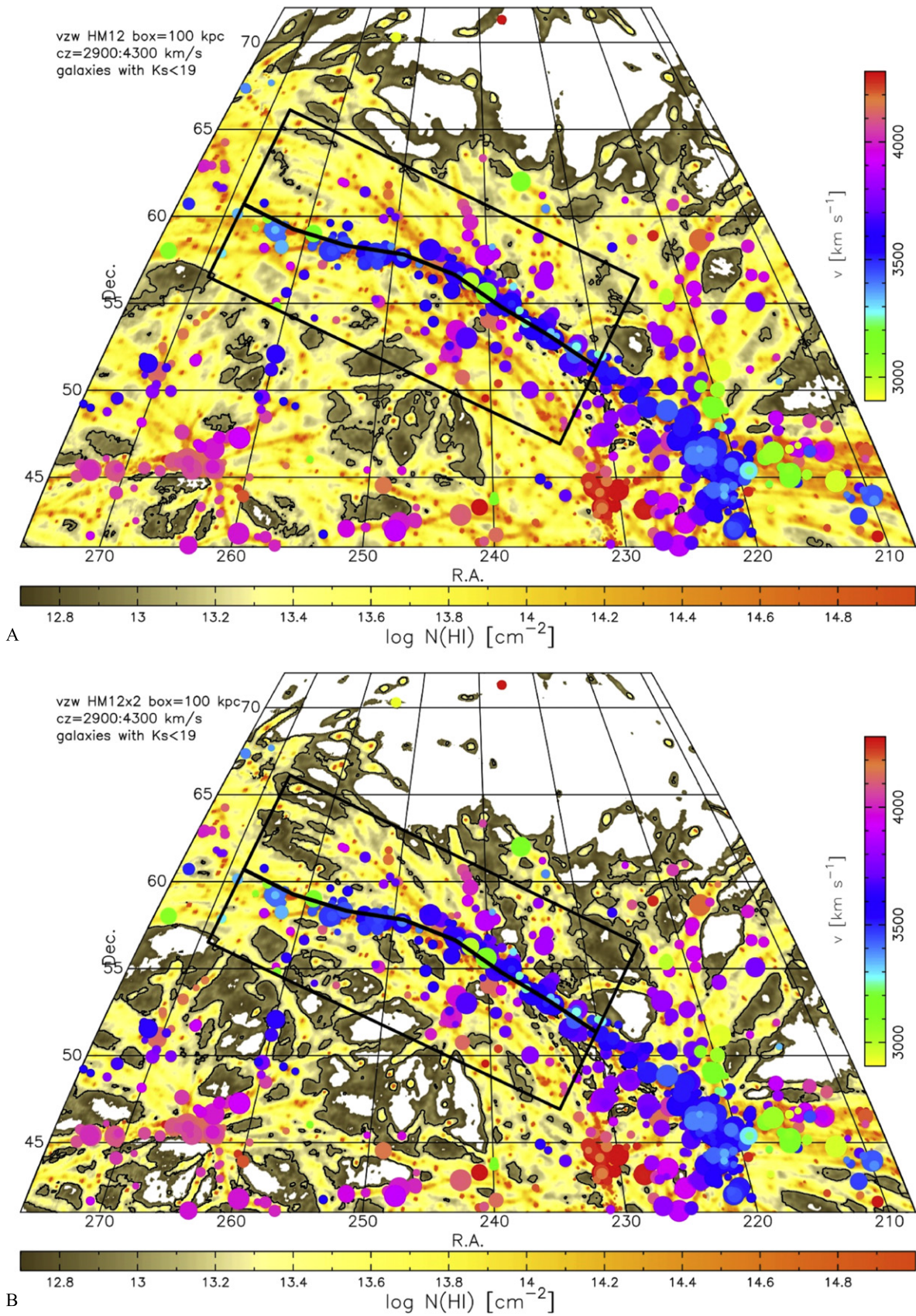


Figure 8. View of the vzw simulation from one viewpoint, with four different versions of the extragalactic background radiation (EGB): Haardt & Madau (2012) (panel a), Haardt & Madau (2012) times 2 (panel b), Haardt & Madau (2001) (panel c), and Haardt & Madau (2001) times 2 (panel d). Otherwise the meaning of the colors, contours, and labels is the same as for Figure 7.

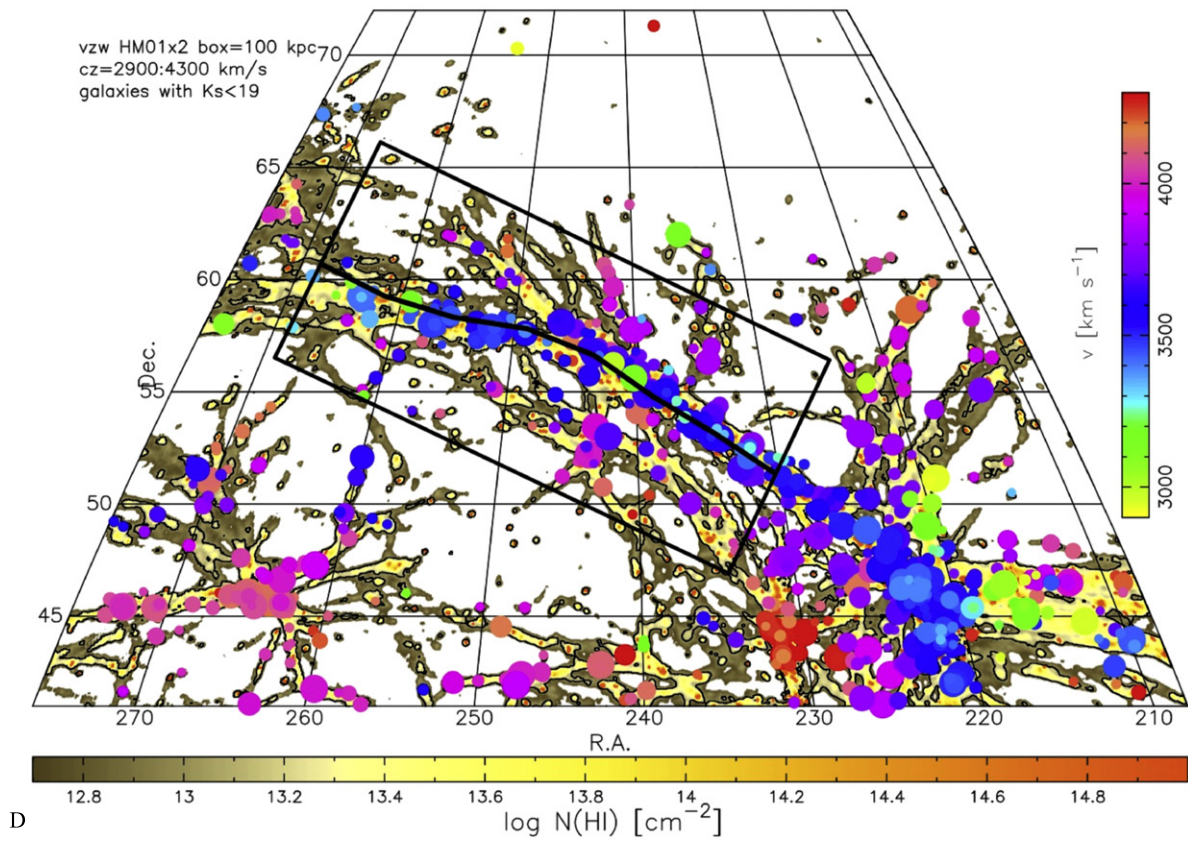
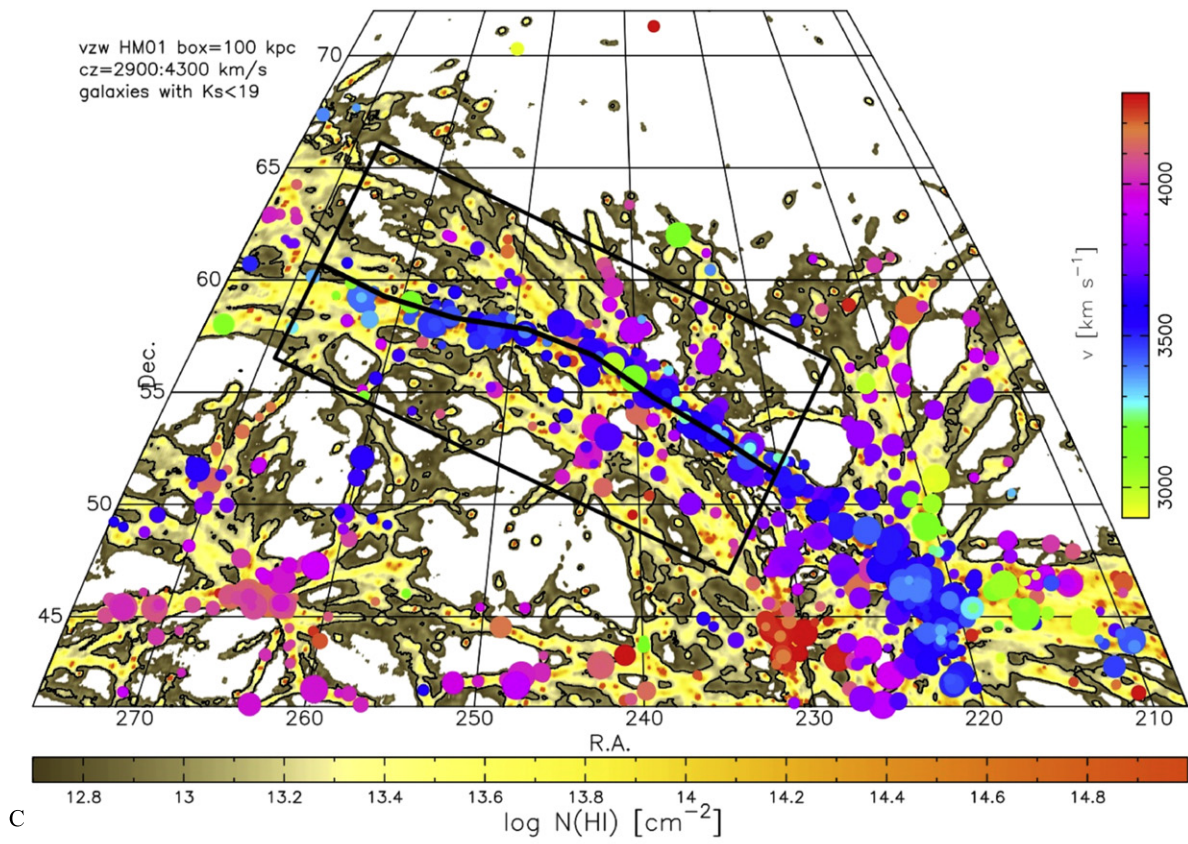


Figure 8. (Continued.)

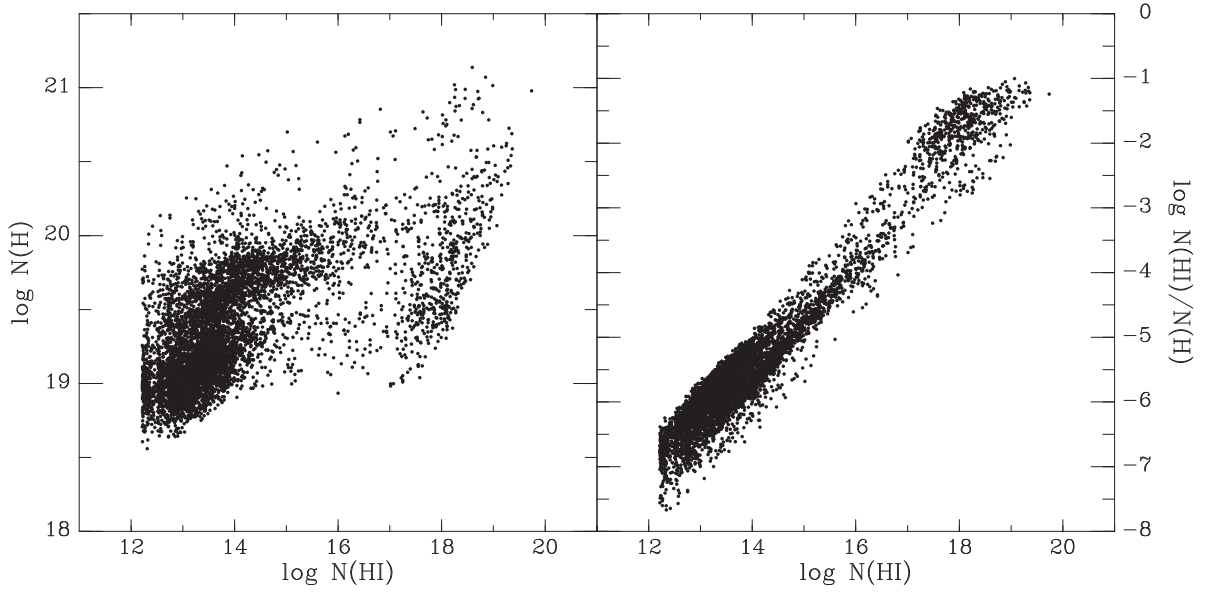


Figure 9. Scatter plot comparing the total baryon column density ($\log N(\text{H})$) against the column density of neutral hydrogen ($\log N(\text{H I})$) for the rectangular box outlining the filament in Figure 7(a) (i.e., the column density when integrating from $cz = 2900$ to 4300 km s^{-1} (a 20 Mpc pathlength), which is dominated by the voxels inside the filament). The concentration of points around $\log N(\text{H I}) \sim 18$ in the left panel corresponds to pixels with a galaxy present. The panel on the right shows how the fraction of hydrogen that is neutral varies with the observed H I column density (i.e., it represents the inverse of the ionization correction).

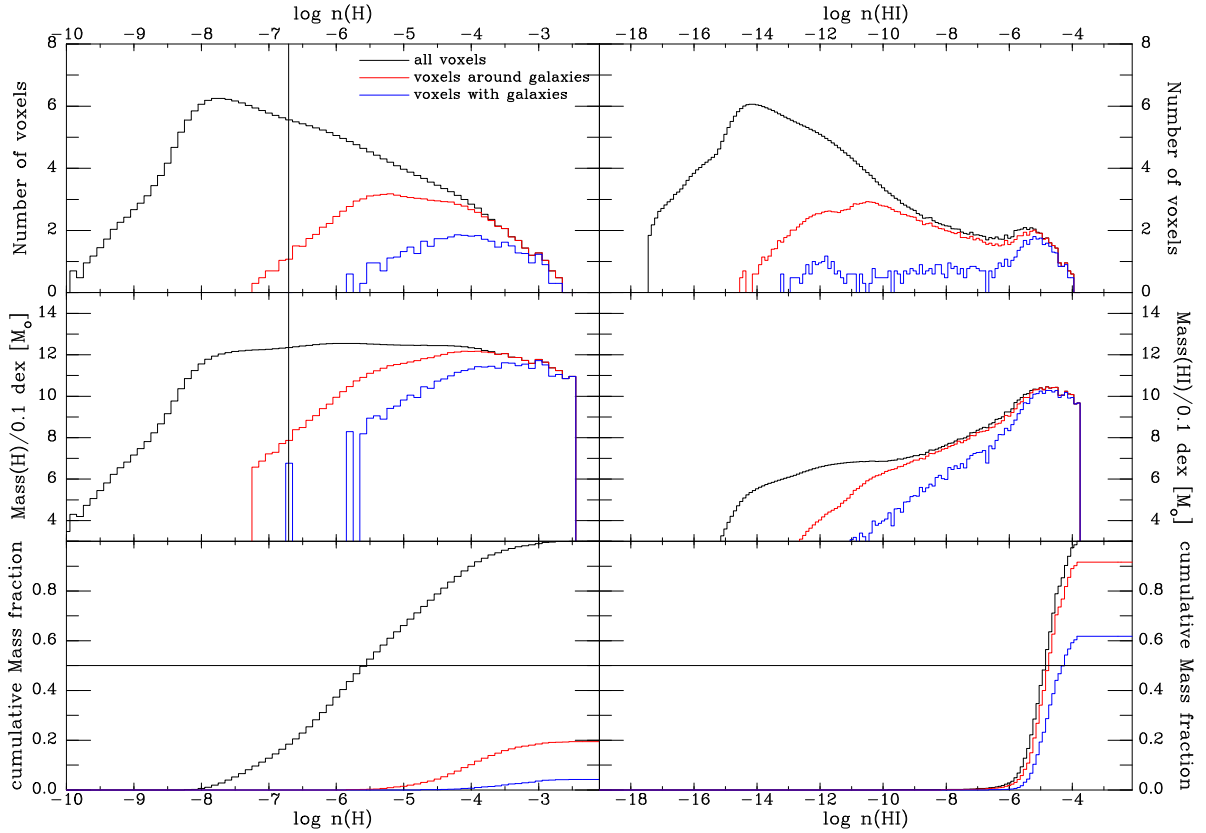


Figure 10. Top panels: number of 100 kpc^3 voxels as function of total or neutral hydrogen volume density in the rectangular box outlining the filament in Figure 7(a). Middle panels: total mass of hydrogen in each 0.1 dex wide bin in $\log n(\text{H})$ (left) or $\log n(\text{H I})$ (right). Bottom panels: cumulative mass fraction as function of volume density. The black curves are for the case that includes all voxels in the box. The blue curves are for voxels in which SKID identified a galaxy, while the red curves are for the 27 voxels around those galaxy-containing voxels (i.e., a $300 \times 300 \times 300 \text{ kpc}$ box). The vertical line in the left two panels indicates the average density of hydrogen ($\log n(\text{H}) = -6.6$, while the vertical line in the right panels indicates the density that corresponds to an H I column density of 10^{13} cm^{-2} in the 20 Mpc deep box.

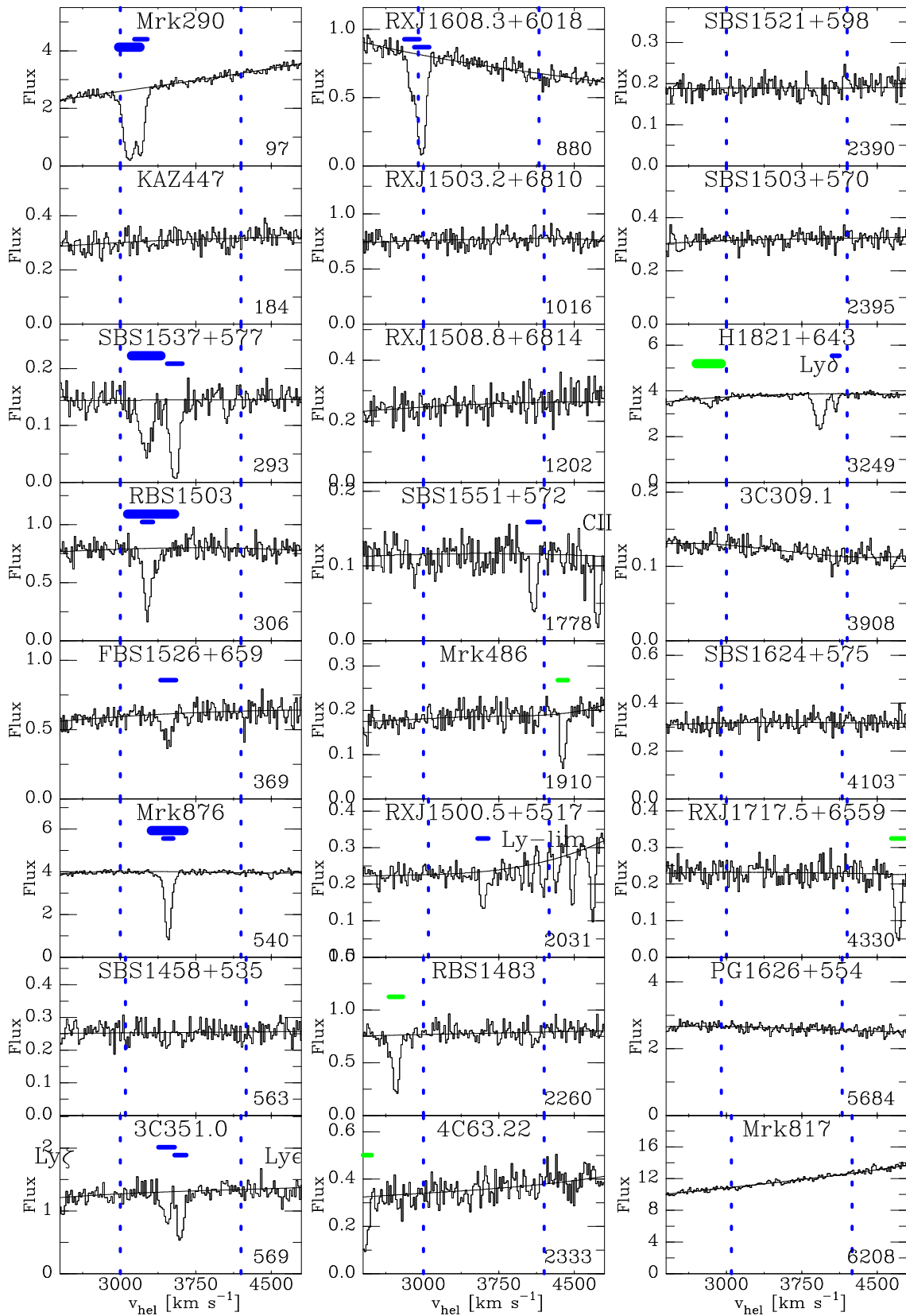


Figure 11. Relevant sections of the COS spectrum for each of the 24 targets analyzed. The targets are sorted by filament impact parameter, given in units of kpc in the bottom right corner. The vertical axis gives the flux in units of $10^{-14} \text{ cm}^{-2} \text{ s}^{-1} \text{ \AA}^{-1}$. All absorption features are Ly α , except for the five labeled Ly δ , Ly ϵ , Ly ζ , Ly-lim, and C III. The blue dashed vertical lines show a 1200 km s^{-1} wide window around the velocity of the nearest filament axis segment (see Section 2). Only lines falling *inside* this window are considered to be associated with the filament. These are indicated with blue horizontal bars above the Ly α absorption. Ly α lines that are not considered to be associated with the filament are indicated by green horizontal bars. The four BLAs are indicated by the thicker blue bars.

Table 3
Ly α Parameters and Detection Limits for Absorption Between 2400 and 4800 km s $^{-1}$

Target	Flux	S/N	ρ (fil)	$v(\text{Ly}\alpha)$	EW	$\log N(\text{H I})$	b	$v(\text{Ly}\alpha)$	$\log N(\text{H I})$	b	Note
(1)	(f.u.)	(3)	(kpc)	($N_a(v)$) (km s $^{-1}$)	(mÅ)	($N_a(v)$) (cm $^{-2}$)	(km s $^{-1}$)	(km s $^{-1}$)	(cm $^{-2}$)	(km s $^{-1}$)	(12)
3C309.1	0.12	13.3	3908		<39	<12.85					
3C351.0	1.28	8.4	569	3596 \pm 2	185 \pm 12	13.68 \pm 0.03	33.1 \pm 2.2	3597 \pm 3	13.77 \pm 0.05	28.9 \pm 4.0	b
				3456 \pm 3	140 \pm 15	13.49 \pm 0.05	44.6 \pm 2.5	3459 \pm 5	13.53 \pm 0.06	39.9 \pm 8.0	
4C63.22	0.33	8.2	2333	2421 \pm 2	228 \pm 26	13.83 \pm 0.07	35.7 \pm 2.7	2420 \pm 4	13.90 \pm 0.08	32.6 \pm 6.3	a
FBS1526+659	0.59	12.0	369	3462 \pm 4	136 \pm 19	13.48 \pm 0.06	46.4 \pm 2.3	3476 \pm 7	13.48 \pm 0.08	38.6 \pm 9.7	
H1821+643	3.72	52.4	3249	2824 \pm 4	44 \pm 4	12.93 \pm 0.04	65.0 \pm 2.2	2825 \pm 6	12.96 \pm 0.04	62.5 \pm 8.4	a
				4087 \pm 2	36 \pm 3	12.86 \pm 0.03	19.4 \pm 2.2	4087 \pm 1	12.91 \pm 0.03	18.7 \pm 2.6	
Kaz447	0.30	11.5	184		<48	<12.94					
Mrk290	2.58	30.4	97	3085 \pm 2	505 \pm 6	14.29 \pm 0.01	56.9 \pm 2.9	3089 \pm 1	14.37 \pm 0.01	52.9 \pm 1.5	
				3202 \pm 2	318 \pm 5	14.04 \pm 0.01	37.8 \pm 3.4	3204 \pm 1	14.07 \pm 0.02	32.1 \pm 1.4	
Mrk486	0.18	10.0	1910	4387 \pm 3	161 \pm 17	13.63 \pm 0.06	25.4 \pm 1.4	4386 \pm 3	13.74 \pm 0.06	25.0 \pm 4.7	a
Mrk817	10.83	47.1	6208		<9	<12.19					
Mrk876	4.00	48.8	540	3472 \pm 2	280 \pm 4	13.90 \pm 0.01	53.2 \pm 3.9	3476 \pm 0	13.92 \pm 0.02	24.7 \pm 0.9	c
								3470 \pm 5	13.22 \pm 0.07	80.9 \pm 11.1	
PG1626+554	2.66	28.6	5684		<21	<12.52					
RBS1483	0.76	11.2	2260	2721 \pm 2	259 \pm 19	13.85 \pm 0.04	44.6 \pm 3.1	2726 \pm 2	13.90 \pm 0.03	35.0 \pm 2.9	a, d
RBS1503	0.78	13.2	306	3272 \pm 2	270 \pm 16	13.88 \pm 0.03	44.1 \pm 2.2	3269 \pm 3	13.81 \pm 0.08	26.9 \pm 5.3	e
				3388 \pm 2	56 \pm 15	13.06 \pm 0.10	39.9 \pm 3.0	3306 \pm 23	13.59 \pm 0.12	116.8 \pm 28.8	
RX J1500.5+5517	0.22	13.8	2031	3595 \pm 2	120 \pm 13	13.44 \pm 0.05	28.0 \pm 2.7	3592 \pm 4	13.51 \pm 0.06	26.8 \pm 6.3	f
RX J1503.2+6810	0.75	12.7	1016		<51	<12.96					
RX J1508.8+6814	0.24	8.0	1202		<102	<13.27					
RX J1608.3+6018	0.81	20.2	880	2983 \pm 4	388 \pm 8	14.15 \pm 0.02	43.0 \pm 2.6	2983 \pm 1	14.26 \pm 0.03	37.0 \pm 2.2	
				2877 \pm 2	117 \pm 10	13.42 \pm 0.04	37.7 \pm 6.0	2886 \pm 5	13.46 \pm 0.06	37.4 \pm 7.0	
RX J1717.5+6559	0.23	9.6	4330	4705 \pm 2	234 \pm 16	13.86 \pm 0.04	29.6 \pm 3.3	4705 \pm 2	13.86 \pm 0.03	32.3 \pm 2.4	a
SBS1458+535	0.25	11.4	563		<57	<12.99					
SBS1503+570	0.31	13.5	2395		<51	<12.94					
SBS1521+598	0.18	10.0	2390		<66	<13.08					
SBS1537+577	0.14	8.8	293	3541 \pm 2	436 \pm 26	14.20 \pm 0.05	49.4 \pm 3.0	3541 \pm 3	14.43 \pm 0.18	37.6 \pm 6.1	
				3260 \pm 2	360 \pm 34	13.98 \pm 0.05	70.9 \pm 3.9	3257 \pm 7	14.03 \pm 0.05	73.2 \pm 9.8	
SBS1551+572	0.11	7.3	1778	4097 \pm 3	195 \pm 21	13.74 \pm 0.07	28.3 \pm 1.6	4097 \pm 5	13.93 \pm 0.10	30.9 \pm 7.6	
SBS1624+575	0.31	12.4	4103		<48	<12.94					

Notes. Col. 1: target name, Col. 2: flux in units of 10^{-14} erg cm $^{-2}$ s $^{-1}$ mÅ $^{-1}$, Col. 3: signal-to-noise-ratio at $cz = 3000$ km s $^{-1}$, Col. 4: cz of Ly α detection as found from $N_a(v)$ integral, Col. 5: equivalent width of Ly α detection, Col. 6: column density of Ly α detection found as the integral of the $N_a(v)$ profile, Col. 7: b -value of Ly α detection found from the second moment of the $N_a(v)$ profile, Col. 8: cz of Ly α detection as found from profile fitting, Col. 9: column density of Ly α detection as found from profile fitting, Col. 10: b -value of Ly α detection as found from profile fitting. Notes: (a) component not considered to be associated with the filament, (b) the 3C351.0 spectrum was taken using the STIS-E140M echelle grating, (c) the very high S/N spectrum of Mrk 876 is best fitted using both a narrow and a broad component, but with the AOD method only a single measurement can be made, (d) this line may have a second component at lower velocities, although a two-component fit is not easily justified—yet the AOD second moment is increased, (e) the properties of the second component are uncertain because it is weak and blended with the stronger component, see discussion in the text, (f) this line lies 0.6 Å above the Lyman limit of an absorber with $\log N(\text{H I}) \sim 16.5$ (i.e., at a wavelength where the individual Lyman lines are blended and weak).

deconvolved this linewidth for instrumental broadening (assuming an instrumental resolution of 20 km s $^{-1}$ FWHM). Second, we used the VPFIT package (see Carswell et al. 2002; Kim et al. 2007) to make a Voigt profile fit to the Ly α lines. VPFIT version 10.2 (<http://www.ast.cam.ac.uk/~rfc/vpfit.html>) was used. The theoretically calculated line-spread function for the COS G130M grating at Lifetime Position 1 (Kriss 2011) was used to convolve with the model fit profile. This line-spread function accounts for both scattering in the far wings due to microroughness in the primary mirror and zonal polishing errors in the primary and secondary mirrors, which results in a COS LSF with reduced core intensity and non-Gaussian strong wings.

Equivalent width detection limits for non-detections were found as three times the error in the equivalent width for a line that is 50 km s $^{-1}$ wide. This was then converted to a column

density detection limit by calculating the $N_a(v)$ integral of a line with the equivalent width equal to the detection limit and an FWHM of 50 km s $^{-1}$. On average this limit is about 10^{13} cm $^{-2}$.

Table 3 presents the measured equivalent widths, column densities, and linewidths determined using both the apparent optical depth and profile fitting methods. For the sake of completeness, the table includes Ly α detections for the extended velocity range shown in Figure 11 (2400 to 4800 km s $^{-1}$). In this figure, the Ly α components that we associate with the galaxy filament are shown by blue horizontal lines extending from $v(\text{Ly}\alpha) - 2b(\text{Ly}\alpha)$ to $v(\text{Ly}\alpha) + 2b(\text{Ly}\alpha)$. Four components can be considered Broad Ly α Absorbers (BLAs; $b > 40$ km s $^{-1}$; see Richter et al. 2004; Lehner et al. 2007). The four components in Table 3 that are not in the velocity range where filament galaxies are found are shown by green horizontal bars.

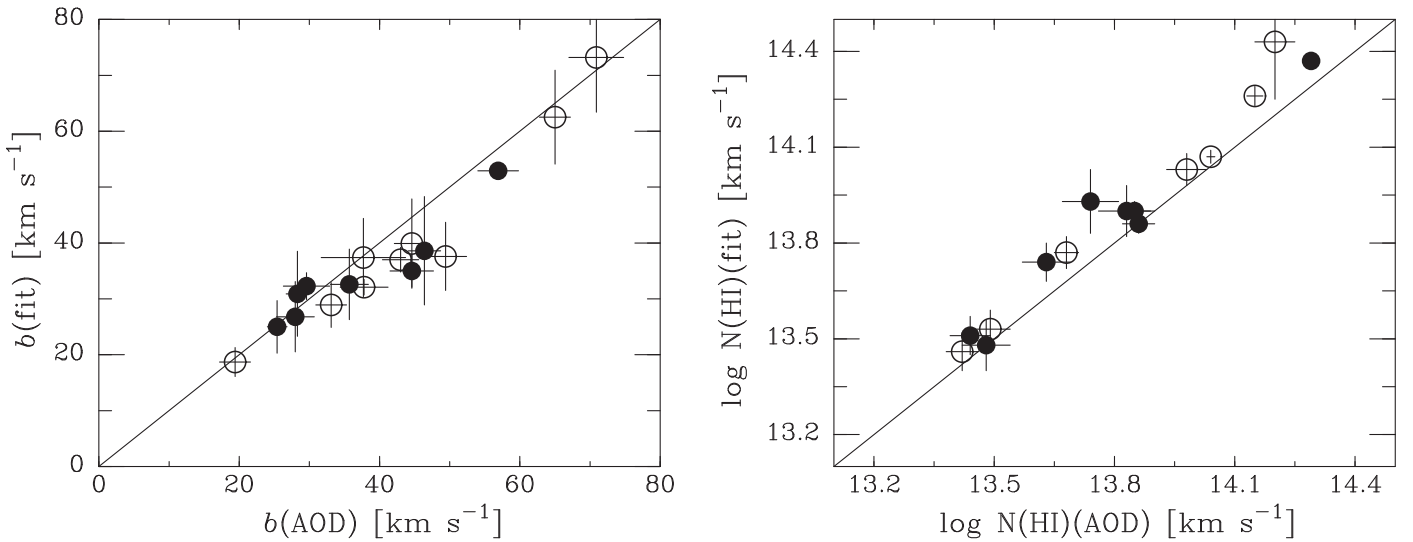


Figure 12. Comparison of linewidth (left) and column density (right) derived using the apparent optical depth (AOD) method (horizontal axes) and Voigt profile fitting (vertical axes). Closed symbols are for single-component Ly α absorption lines, while open circles are for individual components in multi-component lines.

Toward Mrk 290 (filament impact parameter 97 kpc) two components are clearly visible. Associated O VI is also seen in the FUSE spectrum of this target. These components were analyzed in detail by Narayanan et al. (2010), who concluded that they originate from a cloud with $N(\text{H}) = 4 \times 10^{19} \text{ cm}^{-2}$ at $T = 1.4 \times 10^5 \text{ K}$, which is also photoionized. Where Narayanan et al. (2010) focused on a possible association with NGC 5987 (impact parameter 475 kpc; $1.9 R_{\text{vir}}$ see Table 2), it is quite likely that in fact this absorber provides evidence for the presence of WHIM gas in the filament.

The spectrum of Kaz 447 (filament impact parameter 164 kpc) appears to show a small dip near 4300 km s^{-1} . This feature is not significant, however, measuring as 2σ .

For SBS 1537+577, our S/N is insufficient to be sure that the apparent broad component can only be fitted with a single Gaussian or whether it is a combination of two narrower Gaussians. We proceed assuming it is a single broad component.

Toward RBS 1503 two components are clearly present. The profile fitting method gives b -values of 26.9 ± 5.3 and $116.8 \pm 28.8 \text{ km s}^{-1}$, but the two components are heavily blended and the S/N of the spectrum is not sufficient to make a reliable fit. Therefore, in Table 3 we list a very different velocity for the second component in Col. 4 versus Col. 8. This is due to the fact that when using the $N_a(v)$ method we can only measure the line wing, which has a centroid velocity of 3388 km s^{-1} .

The BLA component toward Mrk 876 overlaps with a narrower component at the same velocity, but because the S/N of the spectrum is very high (~ 50), it is clearly significant and not due to the wings on the COS line-spread function.

It is clear from Figure 11 that the strongest and widest absorbers occur toward sightlines passing closest to the filament axis (within 660 kpc), as is the case for multi-component absorbers. The exceptions are a weak line toward FBS 1526+659 and non-detections toward Kaz 447 and SBS 1458+535. The former may be due to the fact that FBS 1526+659 is at the far end of the upper filament and the galaxy density near it is rather low. So even though it is nominally close to the filament axis, it is not in a region with a

lot of gas. In the other two cases we must be looking through a hole, with the Kaz 447 non-detection being especially interesting and revealing small-scale structure because it is close to the sightline to 3C 351.0, where two components are seen.

A map of the galaxies between 1500 and 2900 km s^{-1} shows that the non-filament absorbers toward 4C 63.22, RBS 1483, and H 1821+643 can be associated with another structure, which is clearly visible, but not quite as well defined as the filament shown in Figure 4. Similarly, the component at 4705 km s^{-1} toward RX J1717.5+6559 is at the end of yet another filament that extends from (R.A., decl.) $\sim (260^\circ, 65^\circ)$ to $\sim (240^\circ, 45^\circ)$ with c_z between 5000 and 6200 km s^{-1} . Only the absorber at 4387 km s^{-1} toward Mrk 486 is an orphan that is not clearly associated with any filaments, although it is not too far off from our main filament (off by 1.9 Mpc and 786 km s^{-1}) and a case could be made that it just represents an outlier and should be included.

We note that all our detections have H I column densities below about $\log N(\text{H I}) = 14.5$, whereas absorbers that are associated with galaxy halos typically have higher column densities.

In Figure 12 we compare the column densities and linewidths derived using both the apparent optical depth and profile fitting methods. This reveals that the deconvolved apparent optical depth linewidths are typically wider than those derived from profile fitting—the ratio $b(\text{AOD})/b(\text{fit})$ is 1.08 ± 0.11 . On the other hand, column densities measured using the apparent optical depth method are consistently lower than those found from profile fitting, with $\Delta \log N = 0.07 \pm 0.06 \text{ dex}$. Both of these discrepancies can be understood as a consequence of the non-Gaussian shape of the COS line-spread function (LSF). Because the LSF has strong line wings, the apparent linewidth becomes larger than what it would be if the LSF was a single Gaussian, even after deconvolution. Similarly, the LSF smearing increases the apparent flux in the center of the line, lowering the apparent optical depth. As our comparison shows, this ends up as an about 10% increase in the apparent linewidth and about a 0.1 dex decrease in the derived column density.

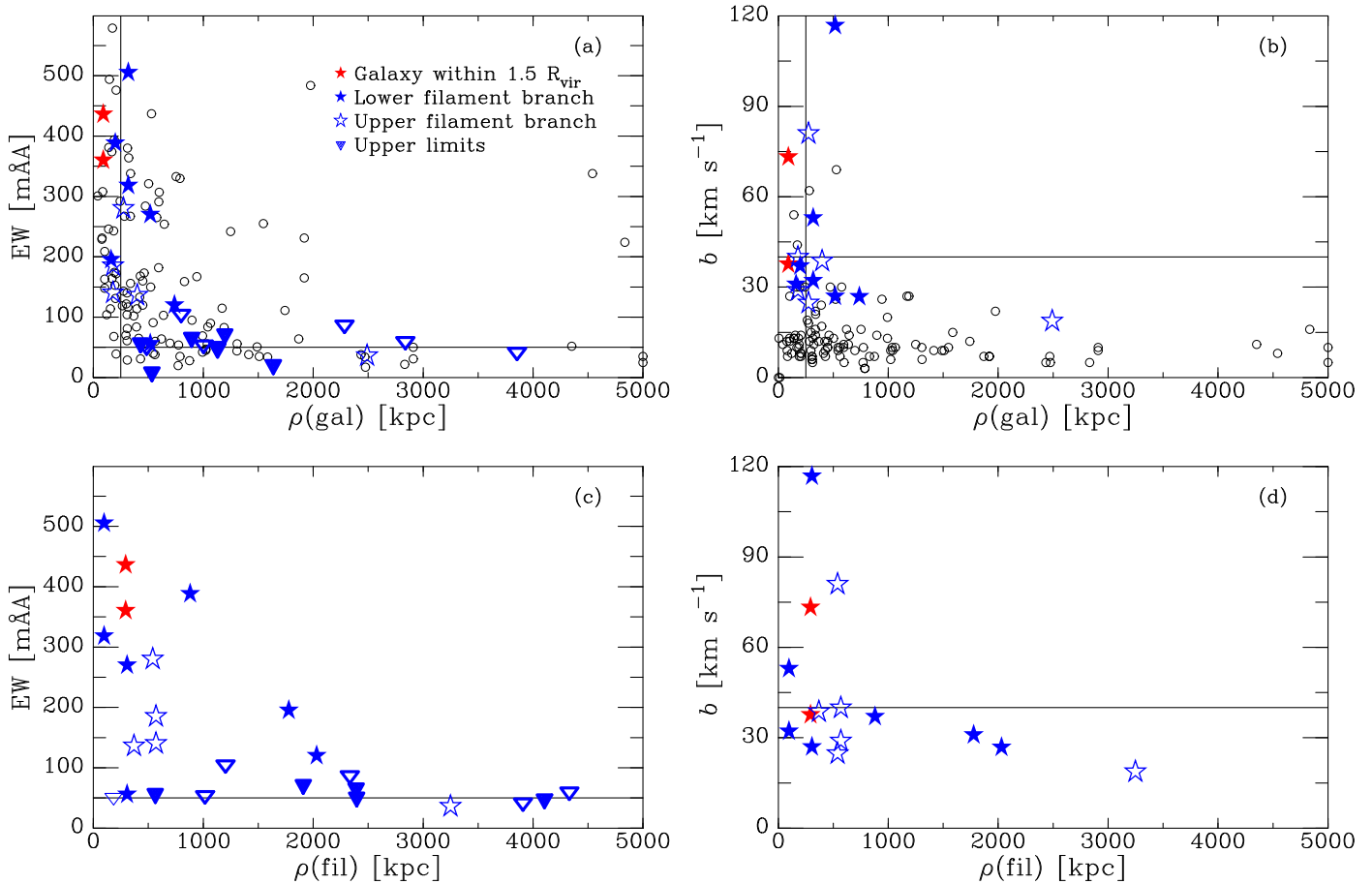


Figure 13. $\text{Ly}\alpha$ equivalent width (left) linewidth (right) vs. filament impact parameter to galaxies (top) and to the filament (bottom). Five sightlines have two components, which are shown separately. For the top panels, the impact parameter is that to the nearest galaxy of any size with velocity within $\pm 500 \text{ km s}^{-1}$ of a $\text{Ly}\alpha$ detection. Open black circles show the results from Wakker & Savage (2009). The red stars are for the two components toward one sightline that passes within one virial radius from a galaxy. The closed blue stars are for sightlines in the “lower branch,” running from (R.A., decl.) = (220, 47) to (247, 64), while open blue stars are for the “upper branch,” running from (270, 60) to (230, 68). Blue downward pointing triangles are upper limits for sightlines with no detected $\text{Ly}\alpha$ in the velocity range 2900–4300 km s^{-1} . The vertical lines in panels (a) and (b) are at an impact parameter of 250 kpc. The horizontal line in the left panels indicates the typical equivalent width detection limit of 50 $\text{m}\text{\AA}$, while the one in the right panels shows the canonical $b = 40 \text{ km s}^{-1}$ separation between narrow and broad lines. Two non-detections from Table 3 are missing in the bottom plot because they have a filament impact parameter $> 5 \text{ Mpc}$. Note that the detection at $\rho(\text{fil}) = 3300 \text{ kpc}$ does not count for the statistic shown in Figure 16 because it has $\log N(\text{H I}) < 13$. The trend of increasing equivalent and linewidth with decreasing filament impact parameter is clear. The exceptions (the points at 50 $\text{m}\text{\AA}$ and 28 km s^{-1} at 400 kpc) come from the multi-component feature toward RBS 1503 that is difficult to fit. Note that for all but four of the blue points, the nearest galaxy is at least 500 kpc distant, or more than $3 R_{\text{vir}}$. For three, the nearest galaxy is at 200–350 kpc (1.5 – $2.5 R_{\text{vir}}$) and the red point is at 91 kpc ($1.0 R_{\text{vir}}$).

5.2. Equivalent Width and Line Width versus Filament Impact Parameter

Using the galaxy and filament impact parameters given in Table 2, we can now plot the distribution of $\text{Ly}\alpha$ lines relative to galaxies and the filament axis. This is done in Figure 13. We use the equivalent width instead of the column density of the $\text{Ly}\alpha$ absorption to facilitate a comparison of the results for the 24 sightlines in this paper with the much larger sample of 125 $\text{Ly}\alpha$ detections given in Wakker & Savage (2009).

The two top panels (a, b) of Figure 13 correspond to the conventional way of analyzing the relation between $\text{Ly}\alpha$ and galaxies. For non-detections we find the galaxy impact parameter as that to the nearest galaxy with velocity between 2900 and 4300 km s^{-1} (i.e., galaxies shown in Figure 4). For $\text{Ly}\alpha$ absorbers the relevant impact parameter is that to the nearest galaxy whose velocity is within $\pm 400 \text{ km s}^{-1}$ of that of the absorber (see Wakker & Savage 2009 for a justification of this number). For Figure 13 we use the impact parameter to the nearest galaxy with $L > 0.1 L_*$, even if there is a fainter galaxy

with slightly smaller impact parameter. As Table 2 shows, there are only four such cases (Mrk 486, SBS 1503+570, SBS 1521+598, and SBS 1624+575), but in all of them the impact parameter to the nearest galaxy with $L > 0.1 L_*$ is not very different. So we effectively avoid the possibly confounding the problem of whether to choose the small impact parameter to a dwarf galaxy or the much larger value to a substantial galaxy.

In this figure, we use a red symbol if the sightline passes within 1.5 virial radii of a galaxy (which happens in just one case, for SBS 1537+577), and a blue symbol otherwise. There are four sightlines (3C 351.0, Mrk 876, RX J1608.3+6018, and SBS 1551+572) where the nearest galaxy is between 150 and 250 kpc, but the impact parameter also is between 1.7 and 2.0 virial radii, so it is not likely that the absorption is associated with the galaxy halo.

Panels (a) and (b) of Figure 13 show that the sample of sightlines in this paper has similar properties as the larger sample in Wakker & Savage (2009); that is, (1) the average equivalent increases for smaller impact parameters; (2) every

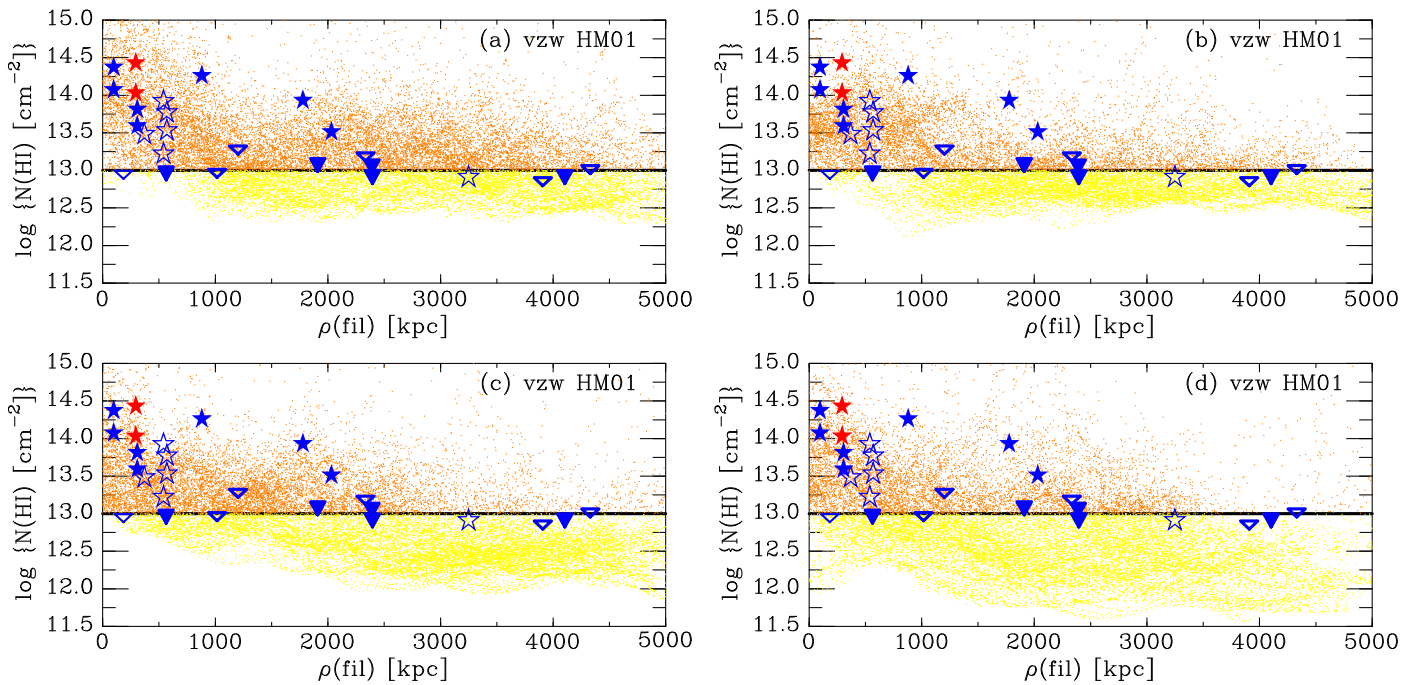


Figure 14. Scatter diagram of H I column density vs. filament impact parameter for the four different viewpoints in the vzw model shown in Figure 7. The nominal Haardt & Madau (2001) EGB prescription was used. Only points inside the rectangular outline box in that figure are shown. Column densities above 10^{13} cm^{-2} are shown by orange points, lower column densities by yellow points. The downward pointing triangles give observed upper limits as function of filament impact parameter, while stars show the detections, with the red star for the sightline within 150 kpc of a galaxy.

sightline with a galaxy impact parameter below 250 kpc shows a Ly α line; (3) for some high equivalent width absorbers the nearest galaxy is separated by more than 250 kpc; (4) non-detections become more common at larger impact parameters; (5) the typical linewidth is larger at smaller impact parameters. Detections at large impact parameters are typically noted, but their properties are mostly ignored because they cannot easily be interpreted in terms of galaxy halos. Such absorbers only play a role when interpreting the column density distribution of Ly α lines in order to estimate the baryon content of the Ly α forest.

Panels (c) and (d) give a different way of looking at these Ly α absorbers and non-detections. Here, the red symbols indicate the components toward SBS 1537+577, which originate at 1.0 times the virial radius from a galaxy and thus conceivably could be associated with that galaxy. The closed blue stars show the components in the lower filament branch seen in Figure 4, while the open blue stars are for the upper branch. It is clear that:

(1) The high equivalent width absorbers occur close to the filament axis, *whether or not there is a galaxy within one virial radius of the sightline.*

(2) There are *no* detections with equivalent width $>50 \text{ m\AA}$ further than 2 Mpc from the filament axis, unlike what is the case in panel (a) where for some absorbers with equivalent width $>100 \text{ m\AA}$ there is no galaxy within 2 Mpc. We note here that the Wakker & Savage (2009) sample with which we make the comparison has a very similar sample of galaxies (basically complete down to $0.1 L_*$ and at $cz < 5000 \text{ km s}^{-1}$.)

(3) In the lower branch (closed blue stars), the largest equivalent widths occur close to the filament, while the smallest equivalent widths occur at large filament impact parameter, in a way that is suggestive of a linear relationship.

However, we will need more data points to confirm that suggestion. Only the broad component toward RBS 1503 ($\rho(\text{fil}) = 373 \text{ kpc}$, $\text{EW} = 56 \text{ m\AA}$) does not follow this pattern, but its equivalent width cannot be measured properly and the linewidth is very uncertain.

(4) The four Ly α absorbers that fit the definition of a BLA ($b > 40 \text{ km s}^{-1}$) all occur in sightlines with two components and only occur at the smallest filament impact parameters. This indicates that the structure of the gas gets more complicated and/or that the gas gets hotter. However, with just four cases out of twelve sightlines, we will need more sightlines and more filaments to make this a statistically sound conclusion.

5.3. $N(\text{H I})$ versus Filament Axis: Observations versus Simulations

To compare observed H I column densities against the simulations, we first show a scatter plot of $N(\text{H I})$ against the filament impact parameter, for four viewpoints for the vzw model (Figure 14) using the HM01 version of the EGB. The four viewpoints are sorted by the density of galaxies along the filament axis (3.8, 2.0, 1.9, and 1.7 galaxies per Mpc for panels a, b, c, and d, respectively). Compare to 2.6 galaxies per Mpc for the observed filament. In Figure 15 we show the effect of varying the EGB for one viewpoint for the vzw model. Observed values are included as colored stars, using the same coding as in Figure 13.

The orange points in Figure 14 represent H I column densities that lie above the average detection limit of the observations (10^{13} cm^{-2} , see Section 5.1), for directions that lie inside the rectangular box outline in Figure 7. The black lines give the 10th, 25th, 50th, 75th, and 90th percentile of column density. The comparison between the different viewpoints shows that there are differences in detail between the four

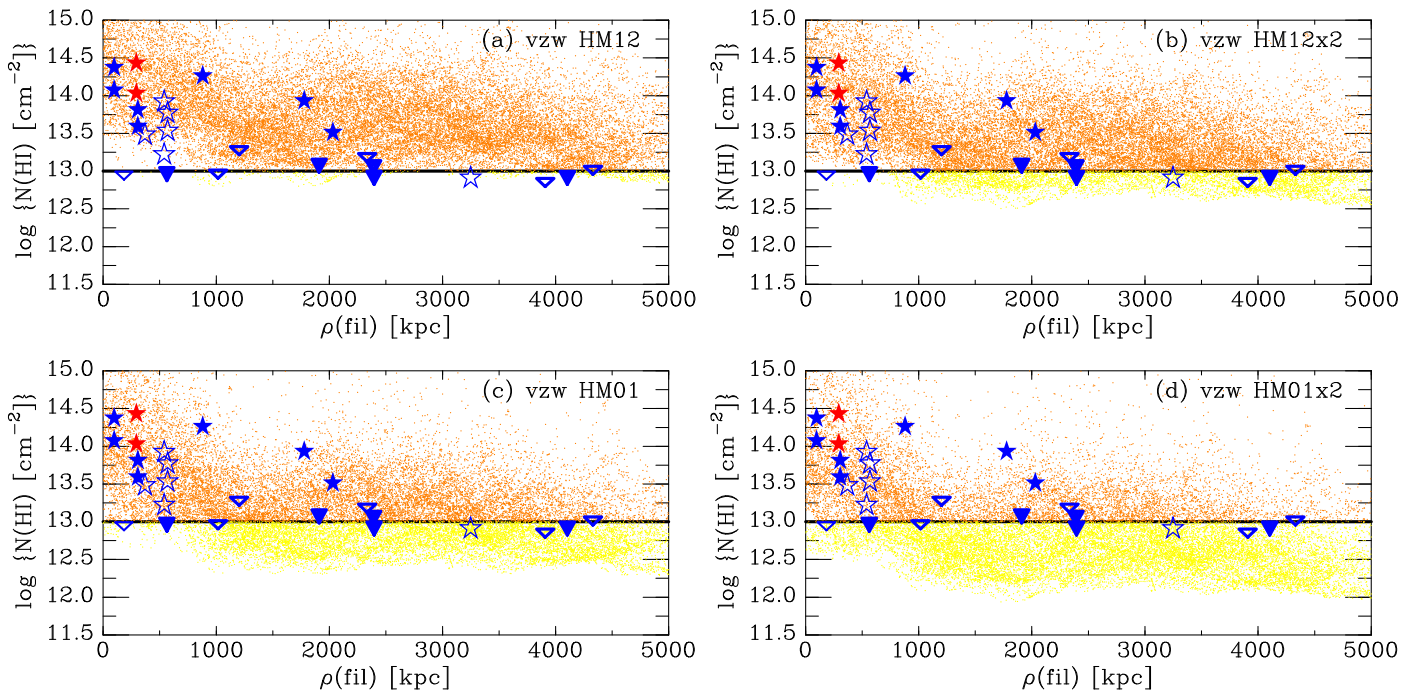


Figure 15. Same as Figure 14, but comparing the vzw model from one viewpoint, with five different versions of the intensity of the EGB, as labeled.

simulated filaments, but in general the column density is always above the detection limit at low filament impact parameters ($< \sim 500$ kpc), while it drops at higher impact parameters. For three of the viewpoints, almost 100% of the sightlines have $N(\text{H I}) > 10^{13} \text{ cm}^{-2}$ at zero impact parameter. Across the filament, the 10th to 90th percentile of column densities have a spread of about a factor of 100. For three viewpoints, column densities $> 10^{13} \text{ cm}^{-2}$ correspond to the 50% or 75% line at several Mpc from the axis, while for one viewpoint the 75% percentile is crossed at 2 Mpc. The observed sightlines appear to provide a fair sample of the expected column densities.

We note here that we adopted the momentum-driven wind (“vzw”) version of the simulation of Oppenheimer & Davé (2008) as a reference, rather than the no-wind, constant-wind, or energy-driven-wind version. However, although in these simulations the galactic winds heat and disturb the IGM close to galaxies, at the Mpc scales of the galaxy filament they have little influence. We did make the equivalent version of Figure 14 using different wind models, but in all cases the distribution of $N(\text{H I})$ versus filament impact parameter is essentially the same, varying only by at most 10% in any individual sightline.

In Figure 15 we analyze the impact of the assumed intensity of the EGB radiation showing the scatter plot of H I column density versus filament impact parameter from the viewpoint shown in Figure 7(a) and the top left in Figure 14 (i.e., the filament with the best match between observed and simulated galaxy density). We use four different versions of the Haardt & Madau model: **HM01** and **HM12**, and both scaled up by a factor two. As expected, the assumed ionizing radiation field has a huge impact on the predicted column densities, with the **HM12** version predicting almost no column densities below 10^{13} cm^{-2} and the **HM01** $\times 2$ version predicting thin filaments at the 10^{13} cm^{-2} level.

5.4. Filament Gas versus Galaxy Mass

Combining our measurements of H I column density with the ionization corrections implied by the simulation, we can estimate the total mass of baryons in the filament. Fitting the relation between the ionization correction and H I column density that is shown in the right panel of Figure 9 yields $\log N(\text{H}) = 0.36 \log N(\text{H I}) + 14.37$, with a typical variation on the order of ± 0.3 dex. Note that this relation is implied when using the **HM01** version of the EGB. The coefficient will change in proportion to the strength of the ionizing radiation field. Using this conversion, the observed H I column densities listed in Table 3 imply total hydrogen column densities ranging from $\log N(\text{H}) = 19.2$ to 19.6 , with an average of 19.35 . We note that for the absorber toward Mrk 290, Narayanan et al. (2010) used the combination of O VI and Ly α and a hybrid ionization model to derive $\log N(\text{H}) = 19.14$. For this cloud the total hydrogen column density implied by the simulation is $\log N(\text{H}) = 19.44$, which is within the ± 0.3 dex range implied by the $\log n(\text{H})$ versus $\log n(\text{H I})$ correlation. If the ionizing background were twice as strong, the two values would match.

In Section 3.2 we estimated the total area of the filament as 170 Mpc^2 . With the average $\log N(\text{H}) = 19.35$ this then implies a total photoionized hydrogen mass in the gaseous filament of $3 \times 10^{13} M_{\odot}$, or $5.2 \times 10^{13} M_{\odot}$ in baryons. Although the line-of-sight thickness of the filament is difficult to specify, it is on the order of 2 Mpc. This then implies a density of the photoionized baryons in the filament of about 15% of the total number of baryons, which is of the right magnitude considering the $\sim 20\%$ – 30% value derived using more sophisticated derivations of the baryon budget (Lehner et al. 2007; Danforth & Shull 2008; Shull et al. 2012) that include both circumgalactic and intergalactic absorbers.

We can compare this to the mass of the galaxies in the filament. This can be derived using the simulated galaxies, from which we find that $\log(\text{mass in } M_{\odot}) = \log(\text{luminosity in } L_{*}) + 11.1$. Combining this with the galaxy luminosities

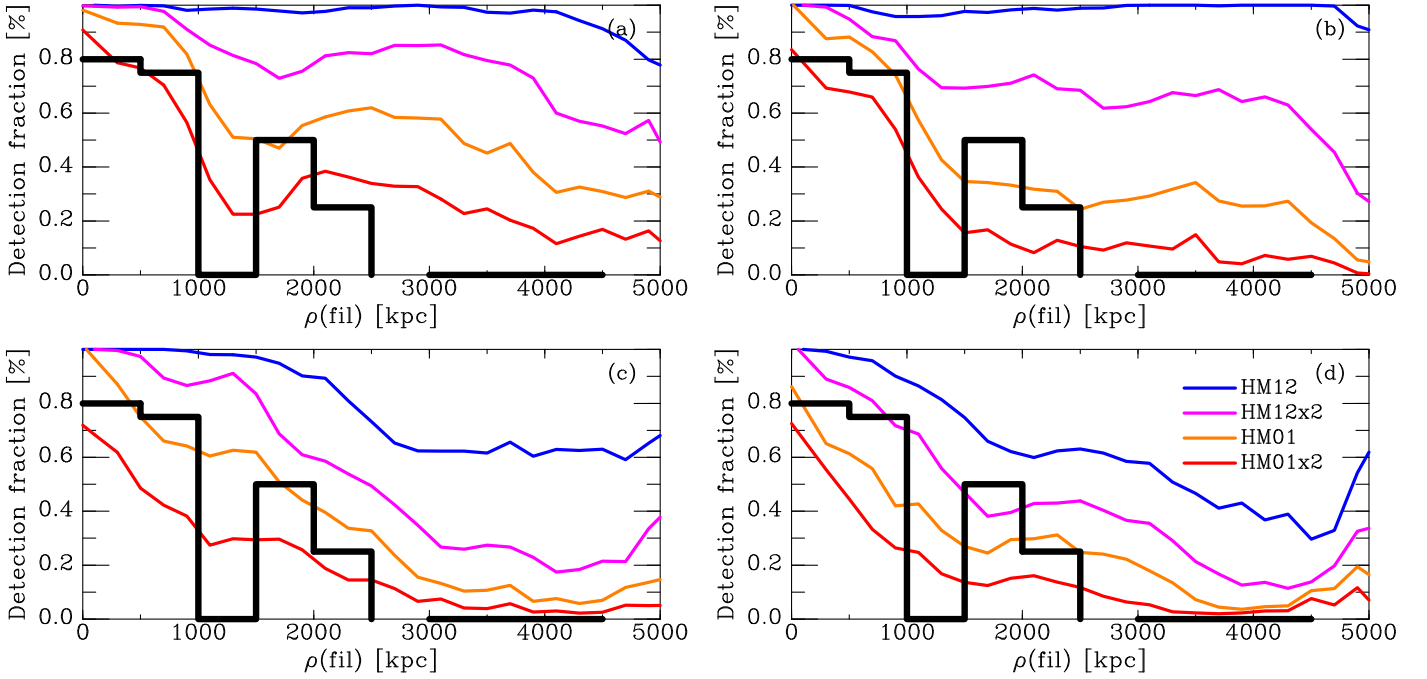


Figure 16. Detection fraction as function of filament impact parameter for different viewpoints inside the simulation cube. Differently colored lines indicate four different versions of the EGB, as shown by the label in the bottom left panel. The detection fraction is the fraction of sightlines in a 200 kpc (for simulations) or 500 kpc (for observations) interval, where $N(\text{H I}) > 10^{13} \text{ cm}^{-2}$. The observed detection fractions (black line) are 80% (4/5) for $\rho = 0\text{--}0.5$ Mpc, 75% (3/4) for $\rho = 0.5\text{--}1$ Mpc, 0% (0/2) for $\rho = 1\text{--}1.5$ Mpc, 50% (1/2) for $\rho = 1.5\text{--}2.0$ Mpc, and 25% (1/4) for $\rho = 2\text{--}2.5$ Mpc. No detections are found for seven sightlines with $\rho = 2.1\text{--}5.0$ Mpc, as indicated by the thick line at zero.

derived in Section 2.1 and adding the implied masses for all galaxies inside the stripe boxes shown in Figure 4 gives a total baryonic galaxy mass of $1.4 \times 10^{13} M_{\odot}$.

Thus, although we use the simulations to derive the conversions between luminosity and mass and between neutral and total hydrogen, scaling the *observed* galaxy luminosities and H I column densities implies that the 21 absorbers in our sample represent four times more baryons than all the baryons inside all the galaxies that were used to define the filament. We previously found that half of the $\text{Ly}\alpha$ absorbers are within 400 kpc of a galaxy (see Table 9 in Wakker & Savage 2009), implying that the baryonic mass of the CGM is comparable to that of the intergalactic gas, and that both are several times more massive than the condensed baryons inside galaxies.

5.5. Detection Fraction

With the limited number of sightlines we have available at the moment, we cannot make the full distribution of column densities in different impact parameter intervals. But we can compare the observed and predicted detection fraction as function of filament impact parameter. This is shown in Figure 16. To make this figure we calculated the fraction of sightlines for which the *vzw* simulation predicts an H I column density above 10^{13} cm^{-2} in intervals of 200 kpc, using the Haardt & Madau (2001, 2012) EGB model. We also calculated the fraction of sightlines for which we detected H I , in intervals of 500 kpc. The 10^{13} cm^{-2} boundary value is the average detection limit for our data (see Section 5.1). In all but two sightlines we are sensitive to $\text{Ly}\alpha$ with $\log N(\text{H I})$ above this limit. There are only six sightlines where the S/N is >20 and the detection limit is lower than $\log N(\text{H I}) = 12.9$, (H 1821+643, Mrk 290, Mrk 817, Mrk 876, PG 1626+554, and RX J1608.3+6018). In this set there is just one H I line with

$\log N(\text{H I})$ below the limit (12.9 toward H 1821+643, see Table 3). For the statistics discussed here, we discount this line because it has $\log N(\text{H I})$ below the 13.0 limit.

The observed detection rate (black histogram in Figure 16) is based on relatively few sightlines, and therefore the detection fraction as function of filament impact parameter remains fairly uncertain. See the figure caption for the percentages and numbers of sightlines. The three robust conclusions that can be drawn are that:

- (1) At filament impact parameters below 1 Mpc the detection rate is high: seven out of nine sightlines show $\text{Ly}\alpha$.
- (2) The detection rate regularly decreases with filament impact parameter.
- (3) No $\text{Ly}\alpha$ lines are found in the seven sightlines with impact parameter >2.1 Mpc.

Comparing the observed detection fraction to the predicted fraction shows that the HM12 model (blue line) grossly overpredicts the number of $\text{Ly}\alpha$ absorbers (i.e., the IGM is underionized in this model). Even scaling it up by a factor of two (magenta line), as proposed by Shull et al. (2015) does not help. The orange line (corresponding to HM01, which has a factor 3.7 more ionizing photons) corresponds much more closely to the observed detection rate at small filament impact parameters (<2 Mpc). However, even then the detection fraction along the axis is predicted to be higher than the observed 80%. Further, some $\text{Ly}\alpha$ lines are expected at filament impact parameters >2 Mpc. For the best matched filaments (a) and (b), the expected probability given the orange and red lines in Figure 16 ranges from $\sim 20\%$ to $\sim 40\%$. Given this expectation, the probability of finding zero detections in a sample of seven ranges from $(1-0.4)^7$ to $(1-0.2)^7$ or $\sim 3\%$ – 20% . Thus, the fact that we do not find any $\text{Ly}\alpha$ lines at a large impact parameter has a low probability.

In summary: the **HM12** version of the EGB has too few ionizing photons, while the shape of the run of the detection fraction with the filament impact parameter may not match the observations.

6. DISCUSSION

From our results it is clear that understanding the majority of Ly α absorbers is best done in terms of large-scale structure, rather than in terms of galaxy halos. Although strong ($N(\text{H I}) > 10^{15} \text{ cm}^{-2}$) absorbers *are* associated with the CGM of galaxies, the weaker Ly α lines are more likely to be associated with filaments. Studies of the galaxy–galaxy versus galaxy–absorber correlation function (e.g., Tejos et al. 2014 and references therein) also indicate that the two differ. As can be seen from Table 2, only one of our sightlines passes within one virial radius of a galaxy (SBS 1537+577 with impact parameter 91 kpc to SDSS J153802.75+573018.3, which has $R_{\text{vir}} = 87$ kpc according to our approximation to the relation of Stocke et al. 2013). In general, we previously found that 50% of Ly α absorbers occur more than 300 kpc away from the nearest galaxy. As Figure 13 shows, however, the properties of Ly α absorbers far from galaxies are not random, but they correlate well with the impact parameter to the galaxy filament that we studied. Not only are the largest equivalent widths seen closest to the filament axis, there is also a hint that the linewidth decreases with filament impact parameter. However, our sample is not large enough to come to a definitive conclusion on this.

With our relatively small sample, the cleanest way to compare observational results to simulations is in terms of the detection fraction. As Figure 16 shows, the fraction of sightlines that show Ly α absorption is maximal near the filament axis and decreases rapidly away from the axis, while no detections are found more than 2.1 Mpc away from the filament axis. Further, the expected decrease in detection fraction depends strongly on the intensity of the ionizing flux in the extragalactic background radiation field (EGB). Using the most sophisticated model that fits the high redshift Ly α forest (Haardt & Madau 2012) yields an ionizing flux that is far too low at $z = 0$, by a factor four to five. This conclusion was previously reached by Kollmeier et al. (2014), who compared the observed column density distribution (from Danforth et al. 2014) with the predictions. Where Shull et al. (2015) found a factor two more intense ionizing flux by using a different hydrodynamical simulation and suggesting a higher escape fraction from galaxies for Lyman continuum photons, Khaire & Srianand (2015) suggest that the contribution from QSOs is twice as high as what Haardt & Madau (2012) found, and propose a 4% Lyman continuum escape fraction to imply an ionizing flux at $z = 0$ that is five times higher than **HM12**.

Our results show that the problem is even more severe, in that the models predict the wrong shape for the run of detection fraction with filament axis. Matching the detection fraction at low impact parameters means that there is too much H I at filament impact parameters > 2 Mpc for simulated filaments (a) and (b), which have a galaxy density similar to that in the observed filament. Matching to the non-detections at large impact parameters means that too few absorbers are predicted at low impact parameters (see, e.g., filament (d) in Figure 16). This could indicate that the ionizing radiation field is even stronger than expected far from filament axis, or that the total

volume density of hydrogen is lower than the simulations predict.

To follow up on this work, we hope to collect other simulations, using different prescriptions for galaxy formation and possibly different predictions for the distribution of the gas around filaments. We are also working to increase our observational sample by analyzing the nine other nearby galaxy filaments that we have located. None of those filaments is sampled by more than 10 sightlines, but cumulatively we will be able to more than double our sample, using COS archival data. It would also be useful to observe of one these filaments with a much denser pattern of sightlines.

7. SUMMARY

We present a study of a local filament in the Ly α forest in three dimensions. We obtained spectra of 24 AGN obtained with the *HST*, and we describe a new method to properly align multiple exposures taken using the COS instrument. We measure the properties of 21 Ly α absorbers with cz between 2400 and 4800 km s^{-1} , seen in 17 of the sightlines. We associate 15 absorbers with a filament of galaxies that is apparent in the distribution on the sky for galaxies with $cz = 2900\text{--}4300 \text{ km s}^{-1}$. We present a method to objectively derive an axis for the filament and analyze the Ly α absorbers with reference to this axis. We also search for similar galaxy filaments in an SPH simulation, and determine filament axes in the same manner as was done for the real sky. We then compare the observed and predicted H I column density as function of the sightline and transverse dimensions for several different prescriptions for the strength of the intergalactic ionizing radiation field. We derive the following conclusions.

7.1. Data Handling

(1) We describe a method to correct the COS wavelength scale that aligns individual exposures without assuming a constant offset, by crosscorrelating all ISM and IGM lines in each exposure. Further, in contrast with other methods that have been described, we properly determine an absolute wavelength scale for the combined spectrum by aligning the ISM lines with a 21 cm spectrum. This prevents smearing of absorption lines in misaligned spectra and allows us to properly assess the alignment of lines in intergalactic absorption-line systems.

(2) An analysis of the error array produced by CALCOS shows that those errors tend to be higher than the errors measured from the rms around a fit to the continuum in the spectra. For target fluxes below $\sim 10^{14} \text{ erg cm}^{-2} \text{ s}^{-1} \text{ \AA}^{-1}$ this results in an overestimation of the errors—on average by 50% for the faintest targets. Thus, using CALCOS errors can lead to large discrepancies when determining the significance of weak lines and of detection limits.

(3) Using the apparent optical depth method to measure column densities and linewidths in COS spectra leads to values that are 10% lower and 10% higher, respectively, when compared to measuring these quantities using profile fitting; the latter more properly takes into account the complex COS line-spread function.

7.2. Properties of Ly α Lines

(4) Our set of sightlines does not generally sample galaxy halos. All but one of the Ly α lines originate far from galaxies

—13 out of 15 absorbers (in 10 sightlines) in our sample do not pass within 1.5 virial radii of any galaxy with luminosity greater than our completeness limit of $0.05 L_*$ (about the luminosity of the SMC). We use 1.5 virial radii as the criterion because this is about the radius at which theoretical considerations (Oort 1970; Maller & Bullock 2004) place the boundary between infalling and intergalactic gas. A fair number of fainter galaxies are also included in our sample, but none is close to a sightline. Using a simple impact parameter limit, three more sightlines with a Ly α absorber pass between 200 and 300 kpc from a galaxy, which is between 1.7 and 2 virial radii. In a very lenient approach, at best these might be classified as sampling the outermost halo of those galaxies.

(5) We use the distribution of galaxies to define a filament at $cz \sim 3500 \text{ km s}^{-1}$. The filament has two branches with sizes $18^\circ \times 7^\circ$ ($\sim 15.5 \times 6 \text{ Mpc}$) and $15^\circ \times 7^\circ$ ($\sim 13 \times 6 \text{ Mpc}$), covering an area of 170 Mpc^2 .

(6) All Ly α lines with $N(\text{H I}) > 10^{13} \text{ cm}^{-2}$ originate within 2.1 Mpc of the filament axis. This includes detections that would be classified as “void” detections in an approach based solely on comparing their location to that of galaxies.

(7) There is a strong correlation between the equivalent width of the Ly α lines and filament impact parameter.

(8) Using the simulations as a guide, we apply an ionization correction to each detected Ly α line and find an average total hydrogen column density of $\log N(\text{H}) = 19.35$. Combining with the area of the filament, this implies a total baryonic mass of $5.2 \times 10^{13} M_\odot$. We also derive the combined mass of the galaxies inside the filament, which is about $1.4 \times 10^{13} M_\odot$.

(9) There is a strong suggestion that the Ly α linewidth correlates with filament impact parameter.

(10) The four broad Ly α components occur only in sightlines that pass close to the axis of the filament (within 400 kpc). Further, multi-component absorbers preferentially occur within about 1 Mpc of the axis. Although the number of sightlines in our sample is small, this strongly suggests an increase in temperature and/or turbulence near the filament axis.

(11) We note that Narayanan et al. (2010) previously found that the BLA toward Mrk 290 containing O VI provides evidence for warm, highly ionized gas in the filament with $N(\text{H})/N(\text{H I}) \sim 1.8 \times 10^3$ and a very large total column density of $1.4 \times 10^{19} \text{ cm}^{-2}$.

7.3. Comparison with Simulations

(12) Using the locations of galaxies in simulations, we can find and define galaxy filaments that resemble the ones seen in the real sky. These filaments are then also seen in the H I column density distribution.

(13) The predicted distribution of H I column density as function of filament impact parameter is strongly dependent on the assumed intensity of the extragalactic background radiation field (EGB). Of the four versions of the Haardt & Madau (2001, 2012) EGB that we tested, we find that the best fit to the data occurs when using their standard 2001 version, in which the contribution to the ionizing flux at $z = 0$ is about the same for quasars and galaxies. This implies that the HM12 model underestimates the ionizing flux by a factor four to five, which is in agreement with Kollmeier et al. (2014). Which is about the factor proposed by Khaire & Srianand (2015), but larger than the factor two proposed by Shull et al. (2015) to match the column density distribution of Ly α absorbers.

(14) Using the best matching EGB, the fraction of sightlines toward which we see Ly α with $N(\text{H I}) > 10^{13} \text{ cm}^{-2}$ matches the simulations only at a small filament impact parameter. For large filament impact parameters ($> 2.1 \text{ Mpc}$) the simulations predict a detection rate of about 20%–40% to find Ly α absorbers with $N(\text{H I}) > 10^{13} \text{ cm}^{-2}$. The fact that we see zero absorbers in seven sightlines may be significant. Given the expected detection rate, the probability of finding zero detections in seven sightlines is 3%–20%. This suggests that there may be a problem with the width of the filaments predicted by the simulations and/or the ionization background is stronger than HM01, although more data is needed.

In summary, we have shown that the properties of the majority of Ly α absorbers can be understood more easily with reference to the large-scale structure of the Cosmic Web, rather than to individual galaxy halos. By analyzing the three-dimensional distribution of Ly α forest absorbers it is possible to constrain simulations, as well as the extragalactic radiation field. More filaments need to be mapped to make our conclusions more statistically robust.

Support for Wakker and Hernandez was provided by NASA through grants *HST*-GO-12276 and *HST*-GO-13444 from the Space Telescope Science Institute, which is operated by the Association of Universities for Research in Astronomy, Incorporated, under NASA contract NAS5-26555. Wakker and French were supported by grant AST-1108913 from the National Science Foundation. Kim acknowledges funding support from the European Research Council Starting Grant “Cosmology with the IGM” through grant GA-257670. Oppenheimer was supported by Space Telescope Science Institute grant *HST*-AR-13262.

APPENDIX

Correcting the COS wavelength scale

As we were preparing COS spectra for a study of O VI absorbers at high S/N (which turned into Savage et al. 2014) we discovered that in many cases the spectral lines in different spectra from the same target did not align, with misalignments of up to $\pm 40 \text{ km s}^{-1}$, and with the misalignment varying as function of wavelength. A summary of the COS wavelength calibration procedure is given by Oliveira et al. (2010). It is based on spectra of six bright targets taken in program 11474 and 11487, tying absorption lines in their spectra to STIS-E140H data of the same targets. The workshop paper states that dispersion relations were derived only using the FP-POS = 3 setting and that a linear dispersion relation was used for the G130M and G160M gratings. Thus, the offsets may be due to the fact that there is no explicit calibration spectrum for every combination of central wavelength and FP-POS settings, so that small distortions in the image on the detector are not accounted for by CALCOS, which assumes the same dispersion relation for different FP-POS settings at the same central wavelength. Offsets can also occur if the target is not at precisely the same spot in the aperture during different visits; this can not be accounted for in the calibration code even in principle. Because the offsets can be as large as a resolution element, this produces an artificial smearing of the lines in the combined spectra. Moreover, absorption lines in a single absorption-line system can appear misaligned.

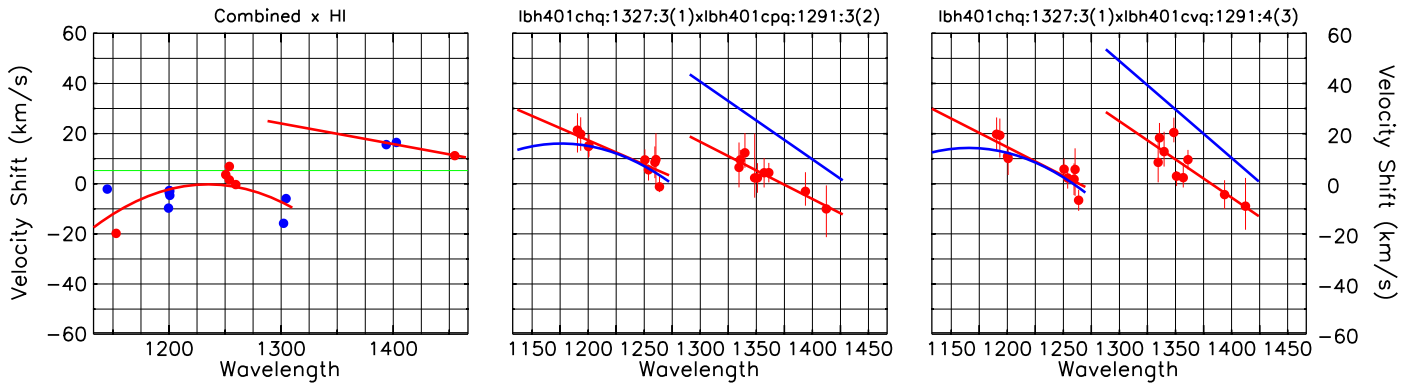


Figure 17. In each panel red points show the cross-correlation offsets for individual absorption lines between a spectrum and the chosen reference spectrum (blue points in panel 1 are for lines with high optical depth for which the centroid determination is more uncertain). The error bars indicate the uncertainties. The left panel gives the differences between the centroids of the ISM lines fitted in the 21 cm spectra vs. the combined UV spectra. The red lines are least-squares fits through these points. The blue lines in the spectrum-vs.-spectrum panels show the final offsets implied for each spectrum, found by combining the relative offsets of the UV spectra with the offset needed to align the spectrum with the 21 cm data. The green line shows the offset needed to bring the nominally calibrated heliocentric velocities in line with LSR velocities. The label (e.g., lbi603o51:1327:3(1)) contains, respectively, the observation ID, central wavelength, FP-POS setting, and exposure ordinal number. Clearly, spectra with 1327:3 show shifts relative to spectra with 1291:3 that vary by up to 60 km s^{-1} across one side.

Other authors have also noticed this issue (e.g., Savage et al. 2011, Meiring et al. 2011, and Tumlinson et al. 2011). They fix the offsets by cross correlating each spectral line separately, determining a centroid and adjusting the wavelengths for each line in each exposure individually. Different lines in the same absorption system are also explicitly forced to be aligned, although that is of course an assumption. Danforth et al. (2014) released a code in which they assume that there is a constant (wavelength-independent) offset between exposures that is determined by a blind cross-correlation of a single 10 \AA wide spectral region around a strong interstellar line, separately for each detector segment (1255–1266 \AA for G130M segment B, 1330–1340 \AA for G130M side A, 1520–1533 \AA for G160M segment B and 1664–1676 \AA for G160M segment A).

Both of these methods suffer from problems, especially for spectra with S/N below ~ 10 . In particular, due to the random noise, the offsets found from cross correlations have uncertainties of a few km s^{-1} , so shifting lines to match their centroids may not yield the correct answer and gives rise to derived shifts that bounce around over short wavelength ranges. When applying the Danforth et al. (2014) method, the shifts are similar to the shifts we find using our method (described below) in most cases, but we have found a few instances where the selected wavelength ranges contain a complicated set of IGM lines and this leads to wildly incorrect shifts—in one case a shift of 100 km s^{-1} was derived. Furthermore, even after aligning in this fashion, the ISM lines in the combined spectra will not always be aligned with the Galactic 21 cm emission, as there may be general offsets in the spectrum chosen to provide the reference wavelengths. Thus, the absolute velocity scale remains suspect.

To solve these problems with wavelength offsets, we instead take the following approach:

(a) First, display all exposures, separately for each grating and each detector side. Then, from the set of ISM lines usually visible in the spectrum (Fe II $\lambda\lambda 1144, 1608$ P II $\lambda 1152, \text{Si II } \lambda\lambda 1190, 1193, 1260, 1304, 1526, \text{Ni } \lambda\lambda\text{-}1199/1199/1200, \text{Si III } \lambda 1206, \text{S II } \lambda\lambda 1250, 1253, 1259, \text{OI } \lambda 1302, \text{Ni II } \lambda\lambda 1317, 1370, 1454, \text{C II } \lambda 1334, \text{C II}^* \lambda 1335, \text{Si IV } \lambda\lambda 1393, 1402, \text{C IV } \lambda\lambda 1548, 1550, \text{Al II } \lambda 1670$) select the ones that are strong and not contaminated by IGM lines. We note that the N I, O I, and Si II-1304 lines are usually not selected

because of the presence of strong geocoronal N I, O I, and O I* emission. To this set we add all strong IGM lines.

(b) Cross-correlate each line in each exposure pair, using a 3 \AA wide region. One spectrum (the first in the list) is chosen as a wavelength reference.

(c) For each exposure, plot the offsets relative to the reference exposure as function of wavelength and fit a first (usually), second (sometimes), or third (if the S/N permits it) order polynomial through these points, separately for side A and B of each grating. This step is illustrated in Figure 17.

(d) Apply the shift as function of wavelength to each spectrum and then combine (see below for more details on this step).

(e) Fit the centroids of interstellar lines that are not saturated, not blended, not too weak, and not otherwise distorted. Well-separated HVCs and IVCs are fitted separately.

(f) Fit the centroid of a 21 cm emission spectrum in the direction of the target, with velocities referenced to the LSR. Comparing the centroids of the 21 cm emission components with those of the ISM lines (see leftmost panel in Figure 17) then gives the wavelength offsets needed to align the reference spectrum. The 21 cm data are from the LAB survey (Kalberla et al. 2005) or the GASS data set (Kalberla et al. 2010). If higher angular resolution data is available, these are used instead. The centroid determination is done separately for weak and strong ISM lines and separately for low- and high-velocity (if any) gas. For strong lines, multiple components can blend. Usually the strong lines are not used in the end, because weak emission components can give substantial absorption components and thus the centroids of emission and absorption no longer align.

This procedure yields a final spectrum with wavelengths such that velocities will be on the LSR scale, which can be converted to a heliocentric wavelength scale. This method works in all cases and does not require the presence of STIS data. Figure 17 shows examples of the offsets as function of wavelength for one of the targets used in this paper.

Combining individual exposures

To combine the aligned spectra, we add the total counts in each pixel and then convert back to flux, using the average flux/count ratio at each wavelength that was used in the original retrieved datafiles. This is the same procedure that was

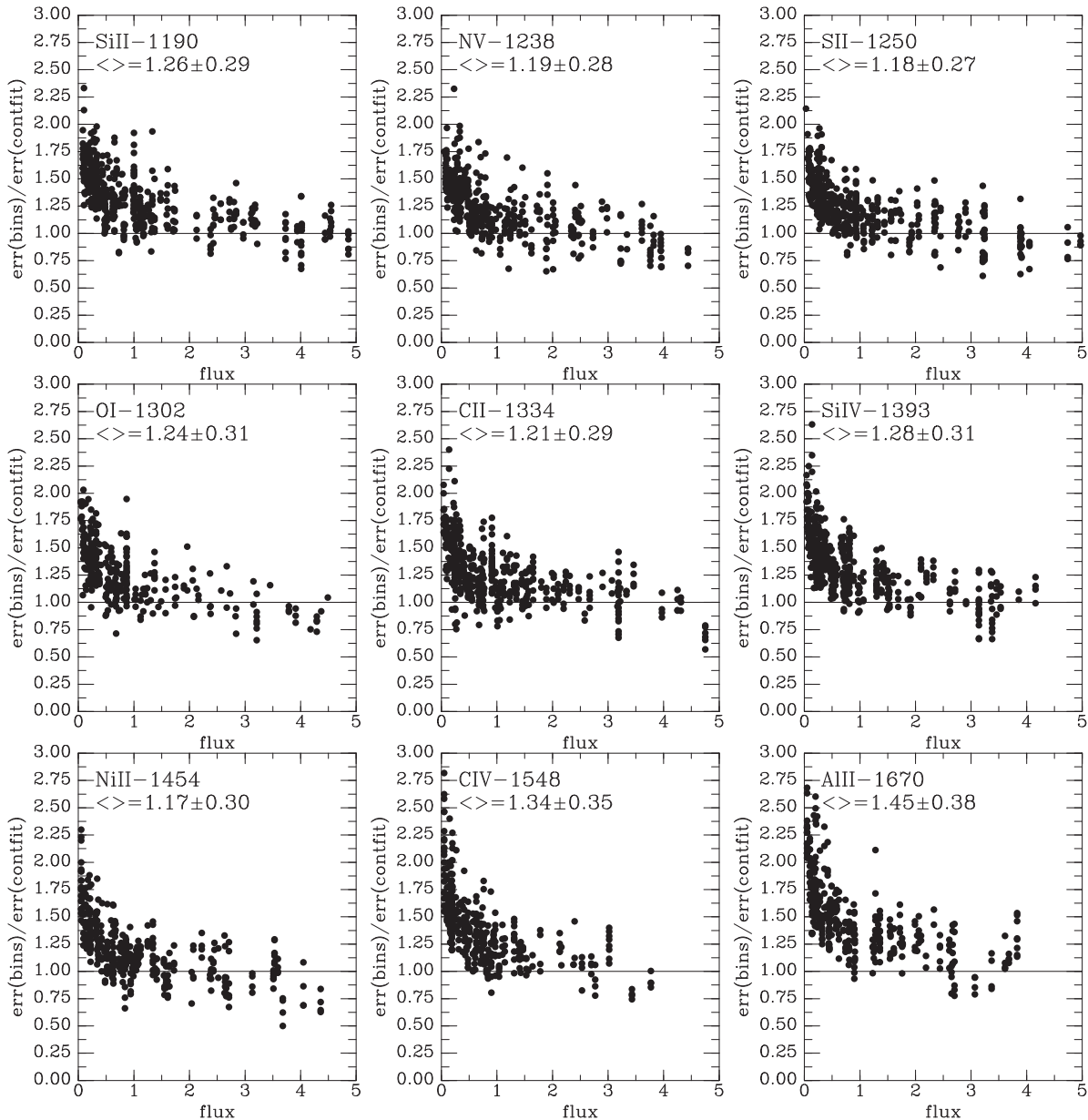


Figure 18. Ratio of fitted error to CALCOS error in individual 1-orbit COS exposures as function of target flux, in units of 10^{-14} erg cm^{-2} s^{-1} \AA^{-1} , near nine ISM absorption lines. The fitted error is found as the rms around the polynomial fit to the continuum, while the CALCOS error is found by averaging the error array in the original data sets over a 300 km s^{-1} wide line-free region near each ISM line. We include only spectra for which a first or second order polynomial suffices, and for which the continuum is relatively flat (variation $<20\%$ in a window several \AA wide).

followed by Meiring et al. (2011) and Tumlinson et al. (2011), but stands in contrast to the procedure of Danforth et al. (2014), who instead calculate an inverse-variance weighted average flux. For cases with equal exposure time for different exposures and non-varying target flux, the different methods give the same answer. However, it is easily shown analytically that if the target flux varies between exposures, the latter method gives the wrong answer. For instance, combining an exposure with one in which the source brightened by a factor two, the inverse-variance-weights give a final flux in the continuum that is $4/3$ times the lower value. However, at low count rates (e.g., in the darker part of spectral lines), the inverse-variance-weight gives a flux more like $3/2$ times the lower value. Thus, this weighting scheme changes the shape of the spectral lines, which is not the case when combining counts.

Error calculation

A study of the error array in the one-dimensional spectra that CALCOS provides revealed that at low fluxes the pipeline gives incorrect numbers. This is found by comparing the CALCOS errors to measured errors. CALCOS errors were calculated as the average of the error arrays in a 300 km s^{-1} wide line-free region near nine ISM absorption lines (in a spectrum rebinned by seven pixels). Measured errors are given by the rms found when fitting a polynomial through the line-free regions near the same nine ISM absorption lines, as well as in spectra binned to seven pixels. Figure 18 shows the ratio of the error array in the datafile to the fitted error. Clearly, for targets with fluxes below $\sim 10^{-14}$ erg cm^{-2} s^{-1} \AA^{-1} the measured rms typically is lower than the value implied by CALCOS, by up to a factor 2 near a flux of

10^{-15} erg cm $^{-2}$ s $^{-1}$ Å $^{-1}$. We have been unable to track down the source of this problem, but it seems possible that at low count rates the CALCOS pipeline overestimates one of the contributions to the error calculation.

We find a better match between calculated and measured error if we just estimate the error from the Poisson noise implied by the total count rate. In that case the calculated and measured error remain similar even at the lowest fluxes. Our final errors are thus calculated using this approach, and ignore the expected, but apparently not actually seen, contributions from dark count, background subtraction, and other such items.

REFERENCES

- Abazajian, K. N., Adelman-McCarthy, J. K., Agüeros, M. A., et al. 2009, *ApJS*, **182**, 543
- Bell, E. F., McIntosh, D. H., Katz, N., & Weinberg, M. D. 2003, *ApJS*, **149**, 289
- Bruzual, G., & Charlot, S. 2003, *MNRAS*, **344**, 1000
- Carswell, R., Schaye, J., & Kim, T.-S. 2002, *ApJ*, **578**, 43
- Cautun, M., van de Weygaert, R., & Jones, B. J. T. 2013, *MNRAS*, **429**, 1286
- Cen, R. 2013, *ApJ*, **770**, 139
- Cen, R., & Ostriker, J. 1999, *ApJ*, **514**, 1
- Chabrier, G. 2003, *PASP*, **115**, 763
- Chen, Y.-C., Ho, S., Freeman, P. E., Genovese, C. R., & Wasserman, L. 2015, arXiv:1501.05303
- Croft, R., Weinberg, D., Katz, N., & Hernquist, L. 1998, *ApJ*, **495**, 44
- Danforth, C. W., & Shull, J. 2008, *ApJ*, **679**, 643
- Danforth, C. W., Tilton, E. M., Shull, J. M., et al. 2014, arXiv:1402.2655
- Davé, R., Cen, R., Ostriker, J. P., et al. 2001, *ApJ*, **552**, 473
- Davé, R., Hernquist, L., Katz, N., & Weinberg, D. H. 1999, *ApJ*, **511**, 521
- Davé, R., Oppenheimer, B. D., Katz, N., Kollmeier, J. A., & Weinberg, D. H. 2010, *MNRAS*, **408**, 2051
- de Vaucouleurs, G., de Vaucouleurs, A., Corwin, H. G., et al. 1991, Third Reference Catalogue of Bright Galaxies (Berlin: Springer)
- Finlator, K., Davé, R., Papovich, C., & Hernquist, L. 2006, *ApJ*, **639**, 672
- Fukugita, M., & Peebles, P. J. E. 2006, *ApJ*, **639**, 590
- Green, J. C., Froning, C. S., Osterman, S., et al. 2012, *ApJ*, **744**, 60
- Haardt, F., & Madau, P. 2001, in Clusters of Galaxies and the High Redshift Universe Observed in X-rays, Recent Results of XMM-Newton and Chandra, XXXVI Rencontres de Moriond, XXI Moriond Astrophysics Meeting, ed. D. M. Neumann & J. T. T. Van (Saclay: CEA), 64
- Haardt, F., & Madau, P. 2012, *ApJ*, **746**, 125
- Jarrett, T. H., ChHester, T., Cutri, R., Schneider, S. E., & Huchra, J. P. 2003, *AJ*, **125**, 525
- Jester, S., Schneider, D. P., Richards, G. T., et al. 2005, *AJ*, **130**, 873
- Kalberla, P. M. W., Burton, W. B., Hartmann, D., et al. 2005, *A&A*, **440**, 775
- Kalberla, P. M. W., McClure Griffiths, N. M., Pisano, D. J., et al. 2010, *A&A*, **512**, 17
- Kereš, D., Katz, N., Weinberg, D. H., & Davé, R. 2005, *MNRAS*, **363**, 2
- Khairé, V., & Srianand, R. 2015, arXiv:1503.07168
- Kim, T.-S., Bolton, J., Viel, M., et al. 2007, *MNRAS*, **382**, 1657
- Kim, T.-S., Partl, A. M., Carswell, R. F., & Müller, V. 2013, *A&A*, **552**, 77
- Kollmeier, J. A., Weinberg, D. H., Oppenheimer, B. D., et al. 2014, *ApJL*, **789**, L32
- Kriss, G. A. 2011, COS IRS 2011–01, http://www.stsci.edu/hst/cos/performance/spectra_resolution/
- Lanzetta, K. M., Bowen, D. V., Tytler, D., & Webb, J. K. 1995, *ApJ*, **442**, 538
- Lee, K.-G., Hennawi, J. F., Spergel, D. N., et al. 2015, *ApJ*, **799**, 196
- Lehner, N., Savage, B. D., Richter, P., et al. 2007, *ApJ*, **658**, 680
- Lukić, Z., Stark, C. W., Nugent, P., et al. 2015, *MNRAS*, **446**, 3697
- Maller, A. H., & Bullock, J. S. 2004, *MNRAS*, **355**, 695
- Marzke, R. O., Huchra, J. P., & Geller, M. J. 1994, *ApJ*, **428**, 43
- Meiring, J. D., Tripp, T. M., Prochaska, J. X., et al. 2011, *ApJ*, **732**, 35
- Morris, S. L., & Januzzi, B. T. 2006, *MNRAS*, **367**, 1261
- Morris, S. L., Weymann, R. J., Dressler, A., et al. 1993, *ApJ*, **419**, 524
- Narayanan, A., Wakker, B. P., Savage, B. D., et al. 2010, *ApJ*, **721**, 960
- Oliveira, C., Beland, S., Keyes, C. T., et al. 2010, in STScI Calibration Workshop, ed. S. Deustua & C. Oliveira (Baltimore, MD: STScI), 408
- Oort, J. H. 1970, *A&A*, **7**, 381
- Oppenheimer, B. D., Davé, R., Kereš, D., et al. 2010, *MNRAS*, **406**, 2325
- Oppenheimer, B. D., & Davé, R. A. 2008, *MNRAS*, **387**, 587
- Paschos, P., Trivedish, Jena, Tytler, D., Kirkman, D., & Norman, M. L. 2009, *MNRAS*, **399**, 1934
- Penton, S., Stocke, J., & Shull, J. 2002, *ApJ*, **565**, 720
- Prochaska, J., Weiner, B., Chen, H.-W., & Mulchaey, J. 2006, *ApJ*, **643**, 680
- Rahmati, A., Pawlik, A. H., Raičević, M., & Schaye, J. 2013, *MNRAS*, **430**, 2427
- Richter, P., Savage, B. D., Tripp, T. M., & Sembach, K. R. 2004, *ApJS*, **153**, 165
- Rudie, G., Steidel, C. C., Shapley, A. E., & Pettini, M. 2013, *ApJ*, **769**, 146
- Rudie, G., Steidel, C. C., Trainor, R. F., et al. 2012, *ApJ*, **750**, 67
- Ryan-Weber, E. V. 2006, *MNRAS*, **367**, 1251
- Savage, B. D., Kim, T.-S., Wakker, B. P., et al. 2014, *ApJ*, **212**, 8
- Savage, B. D., Narayanan, A., Lehner, N., & Wakker, B. P. 2011, *ApJ*, **731**, 14
- Savage, B. D., & Sembach, K. R. 1991, *ApJ*, **379**, 245
- Schaye, J. 2001, *ApJ*, **559**, 507
- Skrutskie, M. F., Cutri, R. M., Stiening, R., et al. 2006, *AJ*, **131**, 1163
- Shull, J. M. 2014, *ApJ*, **784**, 142
- Shull, J. M., Moloney, J., Danforth, C. W., & Tilton, E. M. 2015, arXiv:1502.00637
- Shull, J. M., Smith, B. D., & Danforth, C. 2012, *ApJ*, **759**, 23
- Smith, B. D., Hallman, E. J., Shull, J. M., & O'Shea, B. W. 2011, *ApJ*, **731**, 6
- Sousbie, T. 2011, *MNRAS*, **414**, 350
- Stocke, J., Keeney, B., Danforth, C., et al. 2013, *ApJ*, **763**, 148
- Stocke, J. T., Penton, S. V., Danforth, C. W., et al. 2006, *ApJ*, **641**, 217
- Stone, A. M., Morris, S. L., Crighton, N., & Wilman, R. J. 2010, *MNRAS*, **402**, 2520
- Tejos, N., Morris, S. L., Finn, W., et al. 2014, *MNRAS*, **437**, 2017
- Tejos, N., Prochaska, J. X., Neil, H. M., et al. 2015, arXiv:1506.1031
- Tempel, E., Stoica, R. S., Martinez, V. J., et al. 2014, *MNRAS*, **438**, 3465
- Tripp, T., Sembach, K. R., Bowen, D. V., et al. 2008, *ApJS*, **177**, 39
- Tripp, T. M., Lu, L., & Savage, B. D. 1998, *ApJ*, **508**, 200
- Tumlinson, J., Thom, C., Werk, J. K., et al. 2011, *Sci*, **334**, 948
- Tumlinson, J., Thom, C., Werk, J. K., et al. 2013, *ApJ*, **777**, 59
- Wakker, B. P., & Savage, B. D. 2009, *ApJ*, **182**, 378
- Weymann, R., Januzzi, B., Lu, L., et al. 1998, *ApJ*, **506**, 1